Half of coupling 11-P7C-6F remaining on shaft No. 6 exhibited damage on its fracture surface from contact with the mating coupling half and shaft 5, which likely occurred after fracture event.

End of shaft No. 5 exhibited gouging damage likely from post 11-P7C-6F final failure.

Figure 3-7: Ends of Shaft 5 and 6 Coupled by 11-P7C-6F

Pump P-7A Coupling No. 1 through 8 were submitted to LPI.

Coupling Nos. 4, 5, 6 and 7 (11-P7A-4 through -7) were selected for analysis

Coupling No. 7 (11-P7A-7) shown in its as-received condition.

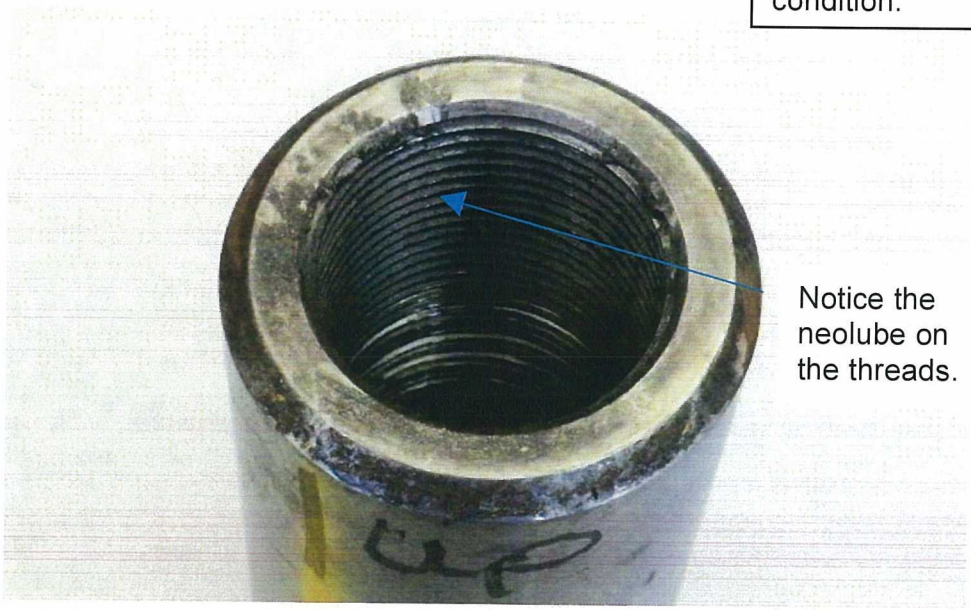

Notice the neolube on the threads.

Figure 3-8: As-Received Coupling No. 11-P7A-7

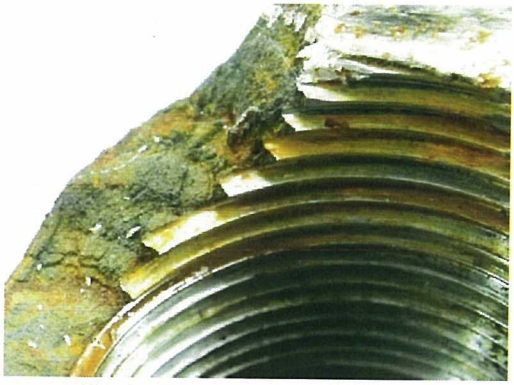

Coupling No. 11-P7C-6F

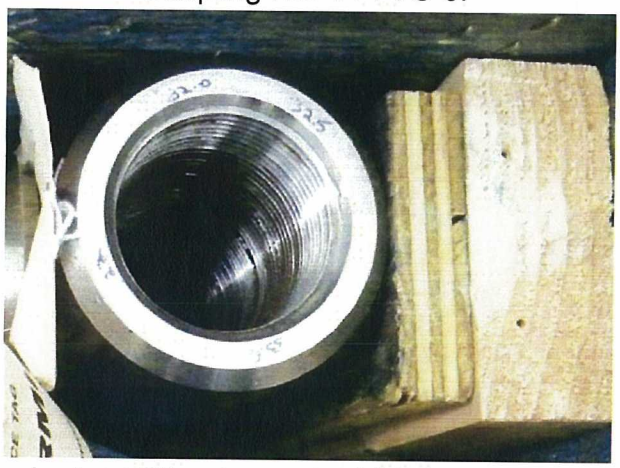

11-P7C-7K in the as-received condition does not exhibit the same level of neolube on threaded surface as 11-P7A-7

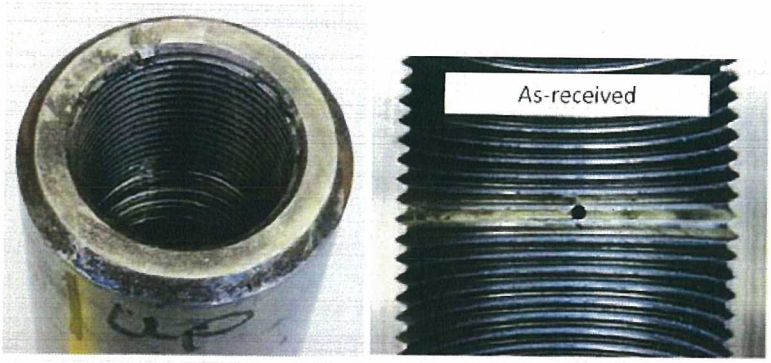

11-P7A-7 in the as-received condition exhibits significant amounts of neolube on thread surface

Figure 3-9: Contrast Thread Coating (As-Received) on P-7C Failed and Cracked Couplings to P-7A Coupling

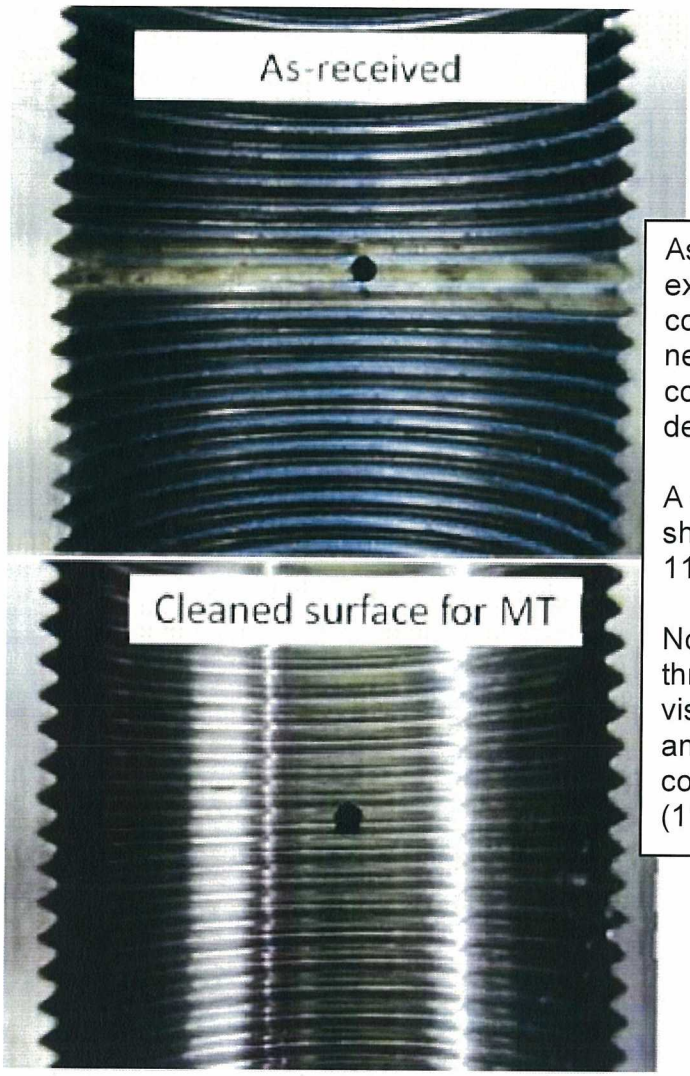

As-received couplings exhibited a greasy grey coating on threads, and near the center of the coupling some surface deposits.

A cleaned surface is shown for coupling No. 11-P7A-5

No cracks along the thread root were visually observed for any of the cleaned couplings (11-P7A-4, 5, 6, 7)

Figure 3-10: Visual Observation of Coupling No. 11-P7A-5

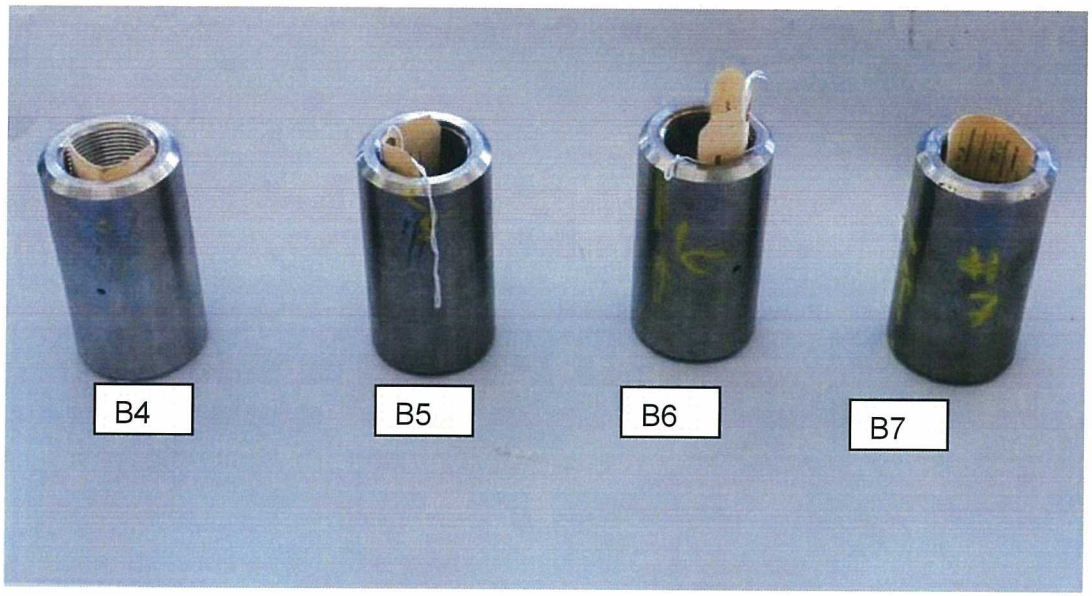

Figure 3-11: As-Received Couplings 11-P7B-4 through 11-P7B-7

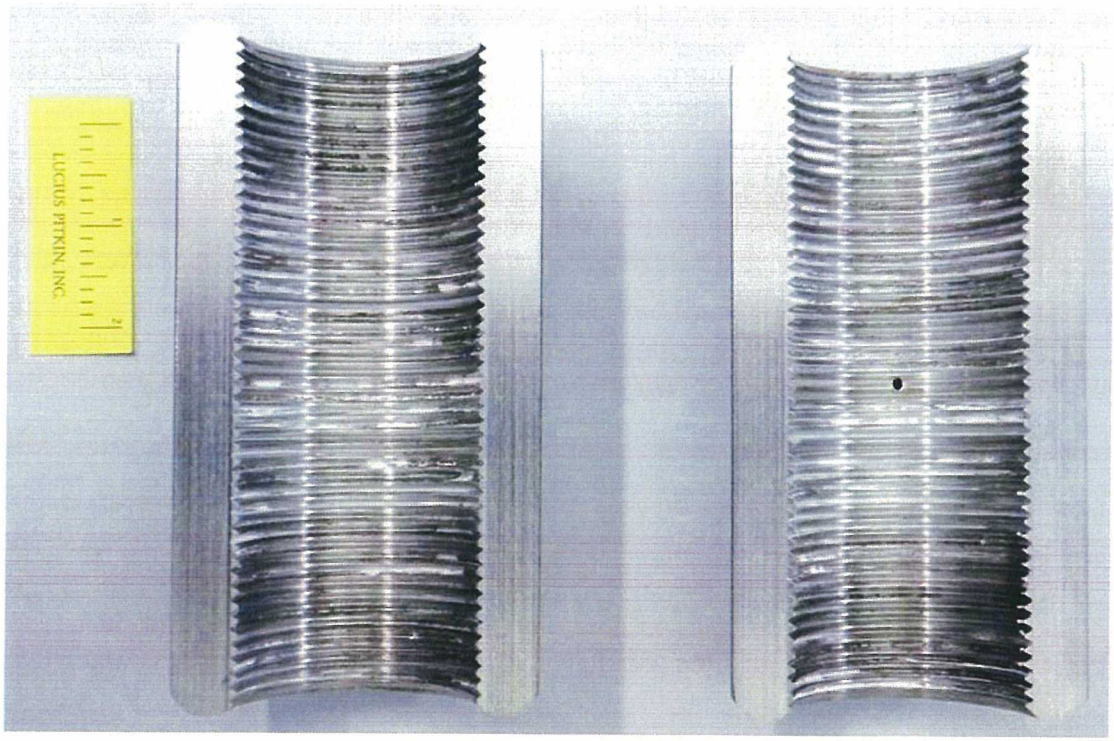

Figure 3-12: As-Split Coupling 11-P7B-4

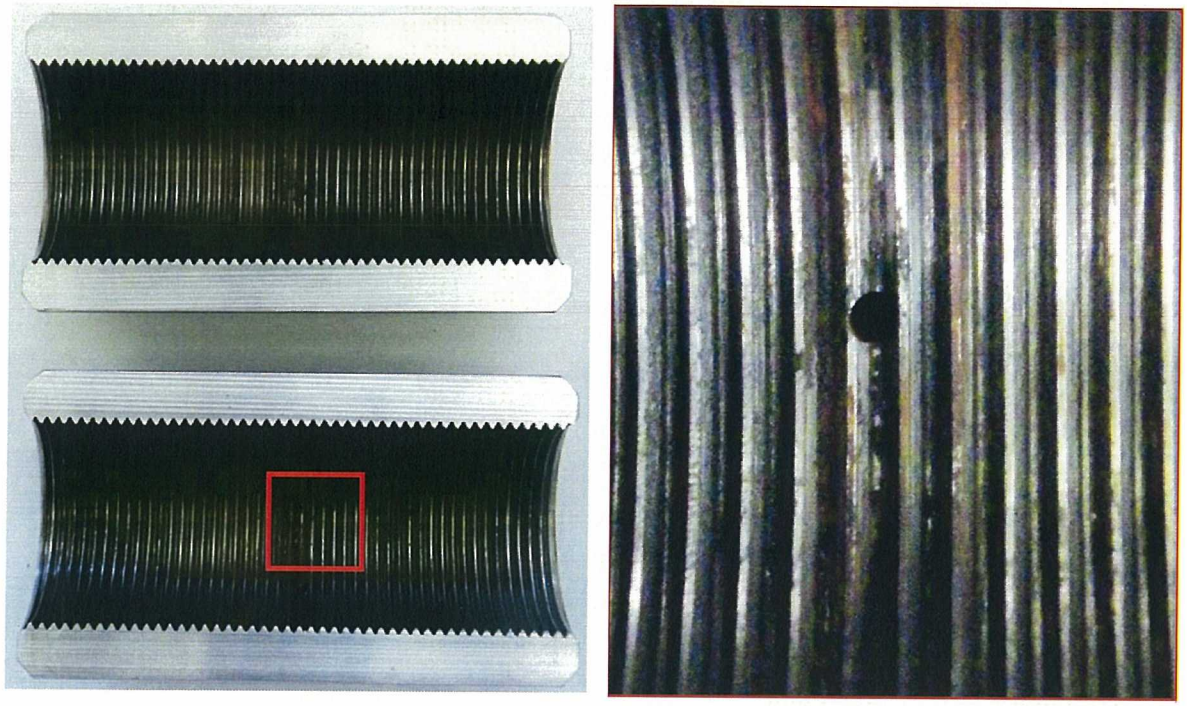

Figure 3-13: As-Split Coupling 11-P7B-5

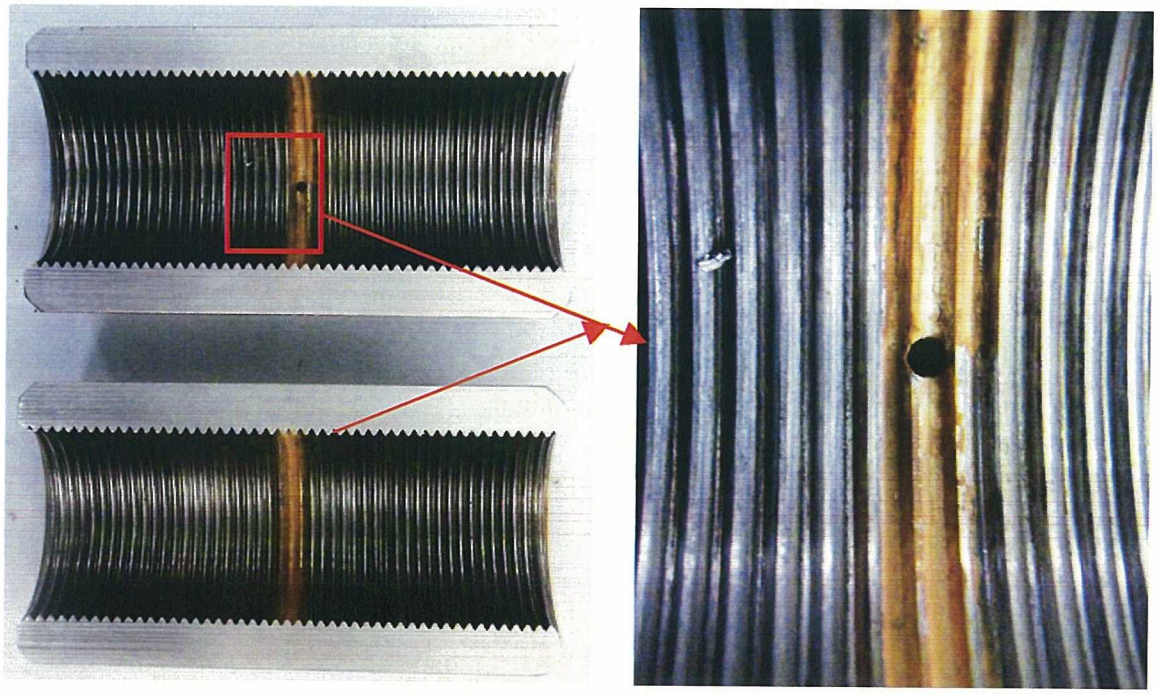

Figure 3-14: As-Split Coupling 11-P7B-6

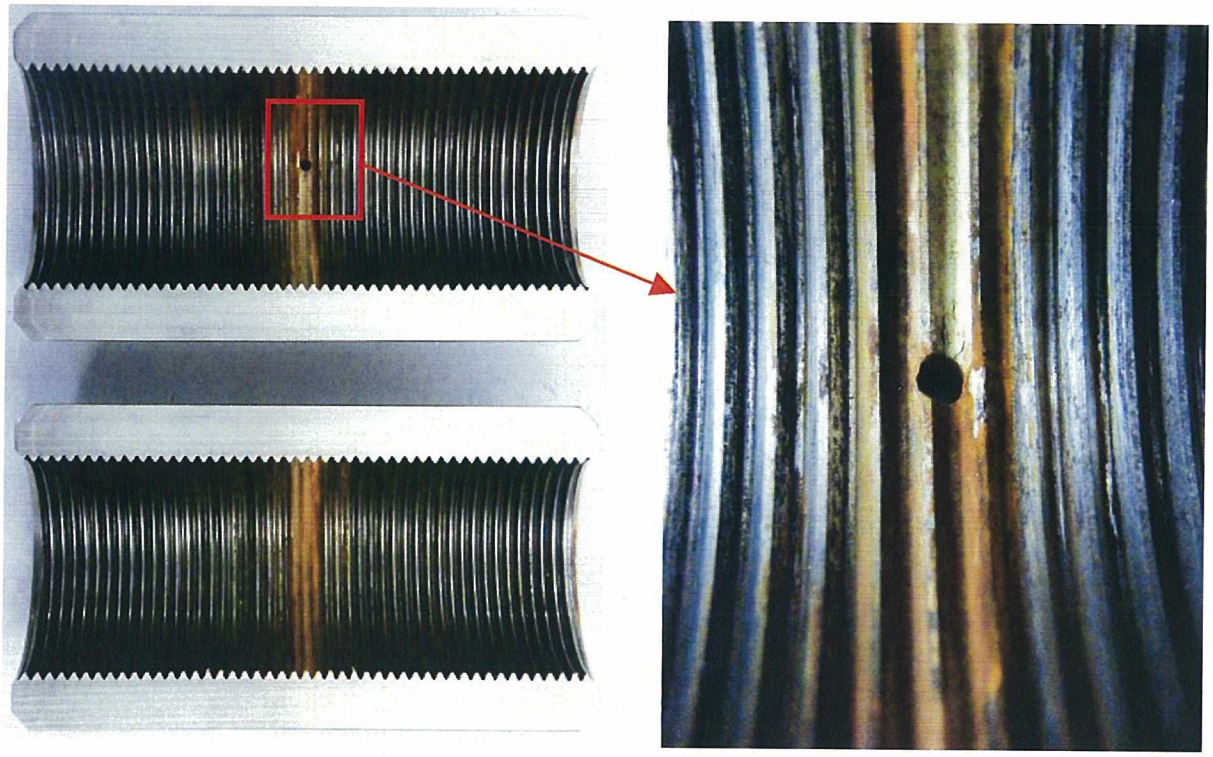

Figure 3-15: As-Split Coupling 11-P7B-7

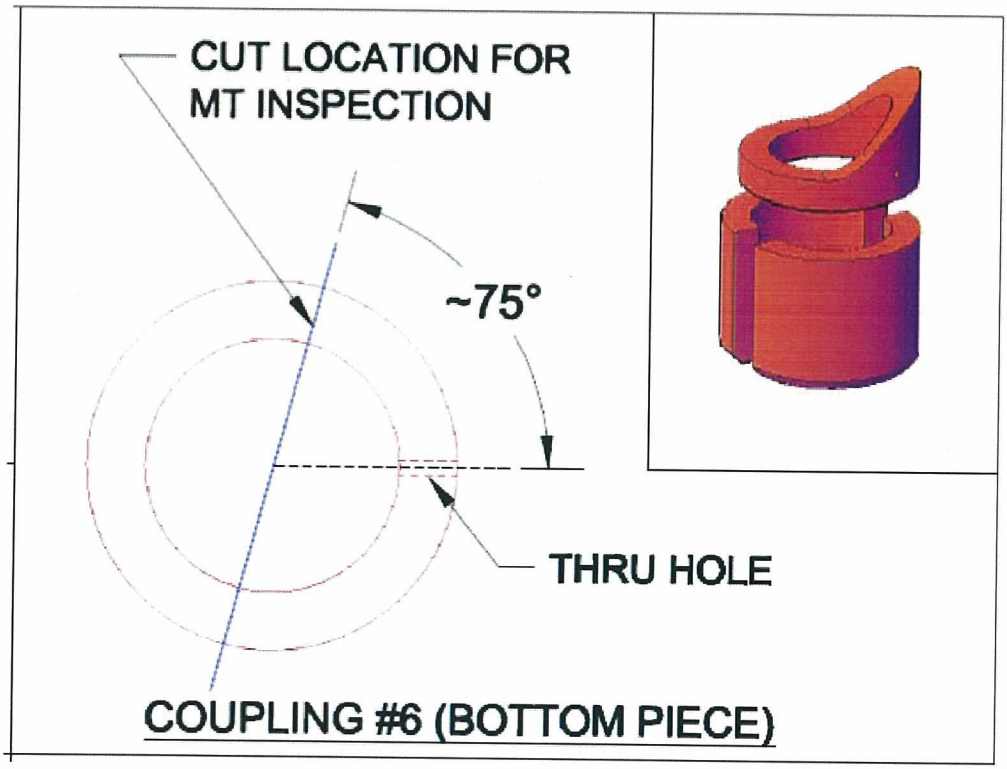

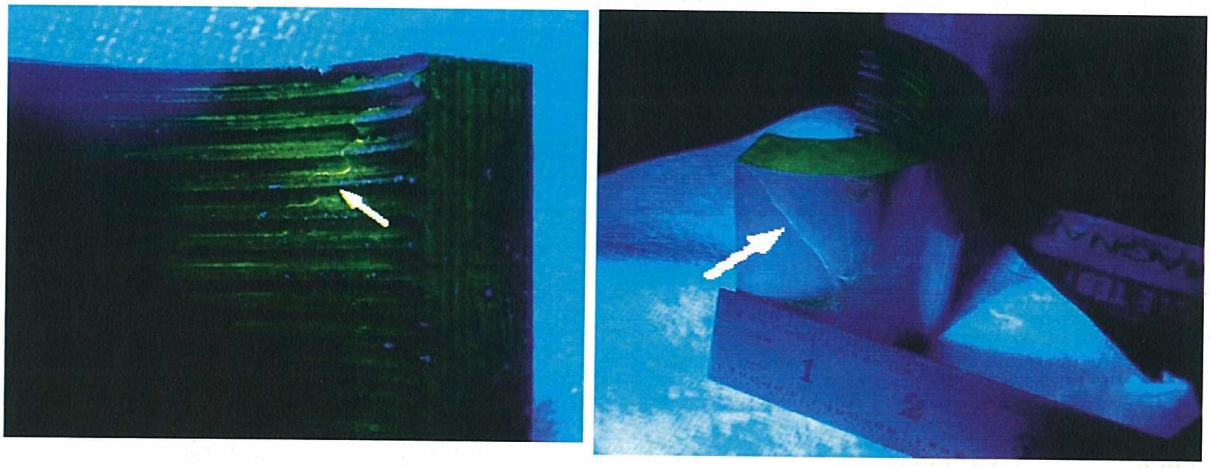

After fracture surface was sectioned, a remaining portion of coupling 11-P7C-6F was MT inspected. Arrows show location of indications.

Figure 3-16: MT Highlighting Un-Opened Fracture on Coupling 11-P7C-6F

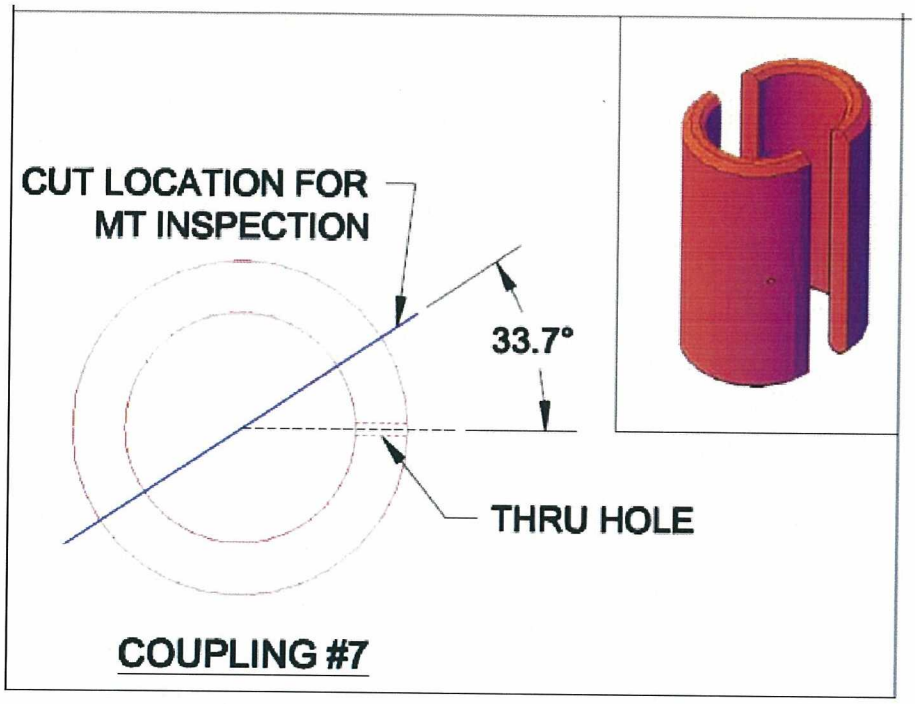

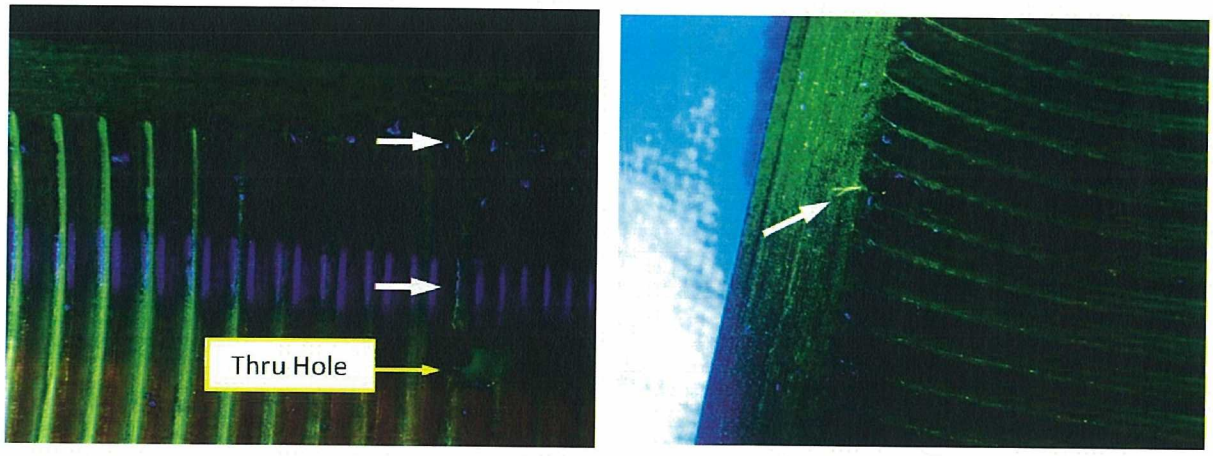

Top sketch show the cut line for coupling 11-P7C-7. Fluorescent MT examination of this coupling reveals an indication, shown by a well-defined fluorescent line, initiating from a thread root and propagating in the radial direction. The left and right images show the same indication on the two sections of this coupling after cutting in half longitudinally. Arrows show location of the indication.

Figure 3-17: MT Highlighting Crack on Coupling 11-P7C-7K

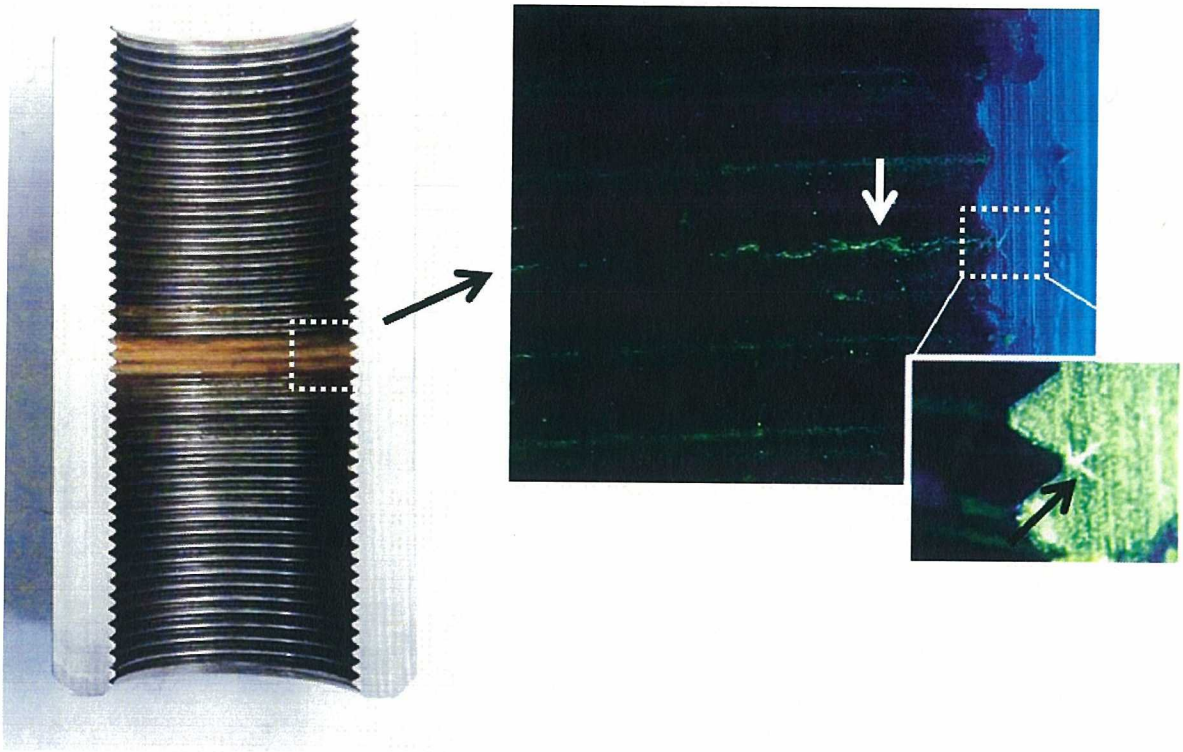

Figure 3-18: MT Highlighting Crack on Coupling 11-P7B-7K

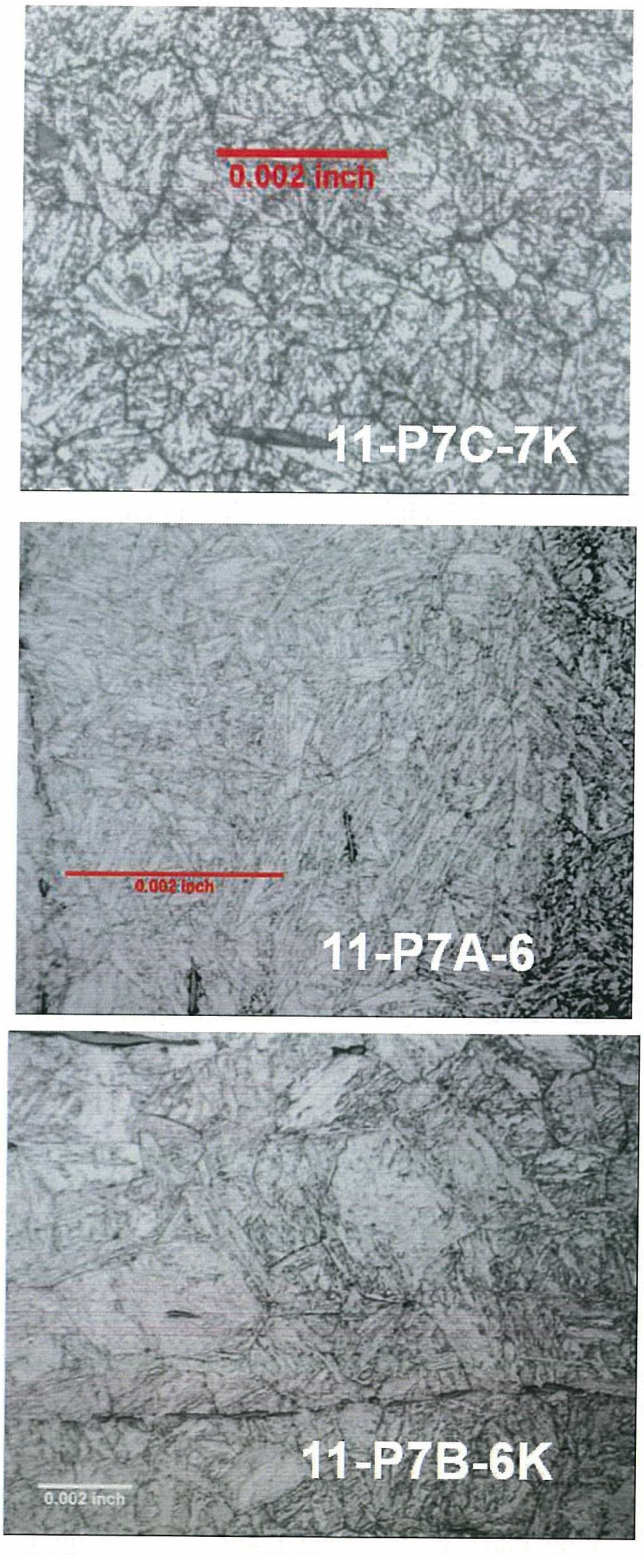

Figure 3-19: General microstructure of coupling material

As-polished condition and viewed at 50x.

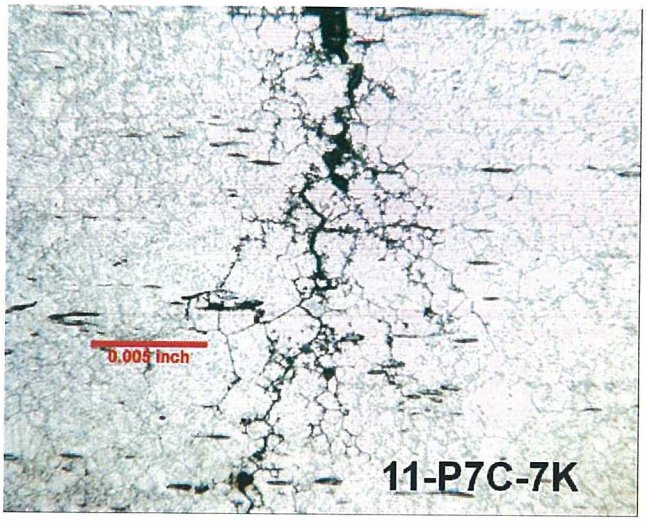

Etched condition viewed at 200x.

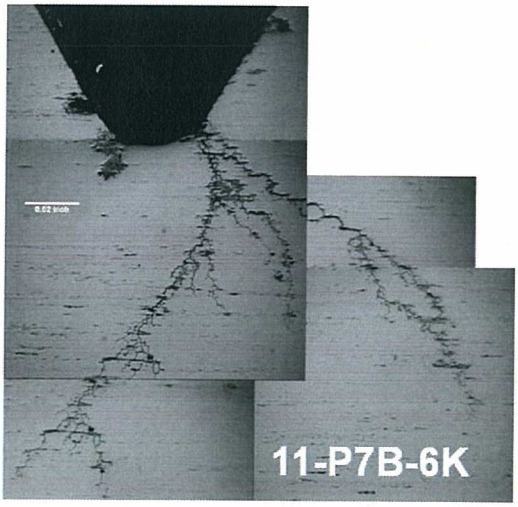

As-polished condition
50X, scale bar 0.02 in.

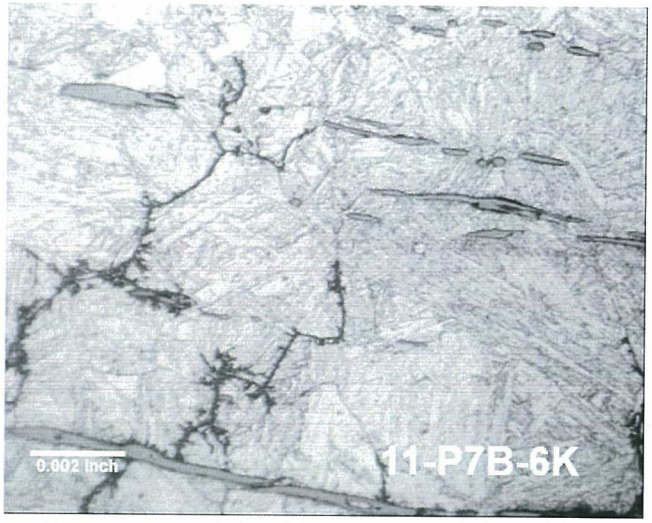

Etched condition, 400X, scale bar 0.002 in.)

Images of SCC cracks in coupling 11-P7C-7K (top) and 11-P7B-6K (bottom) showing the network of cracks that follow the prior austenite grain boundaries.

Figure 3-20: As-polished (left) and Etched (right) Microscopy

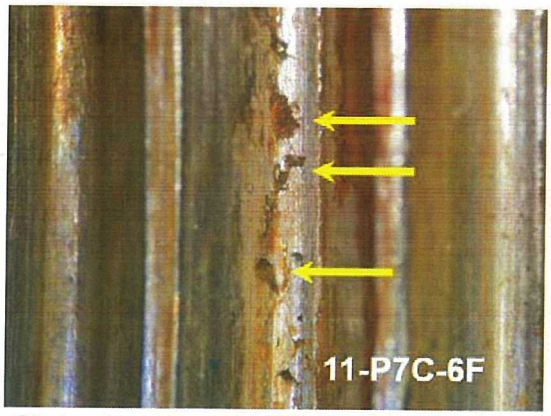

Pitting at root near middle of fractured Coupling No. 6 (Stereomicroscopy 15X)

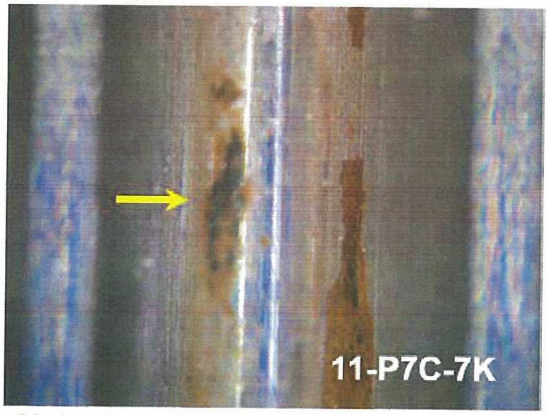

Pitting near the root and near middle of Coupling No. 7 (Stereomicroscopy 40X)

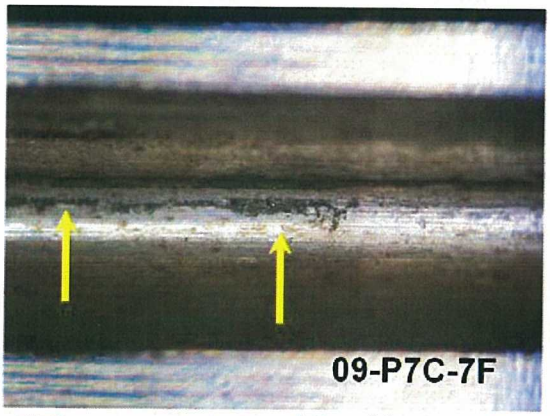

Pitting near root at middle of fractured Coupling No. 7 from 2009 event (Stereomicroscopy 30X)

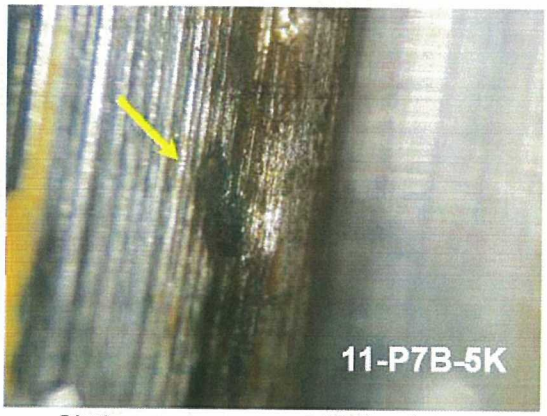

Pitting near root at middle of Coupling No. 5 (Stereomicroscopy 40X)

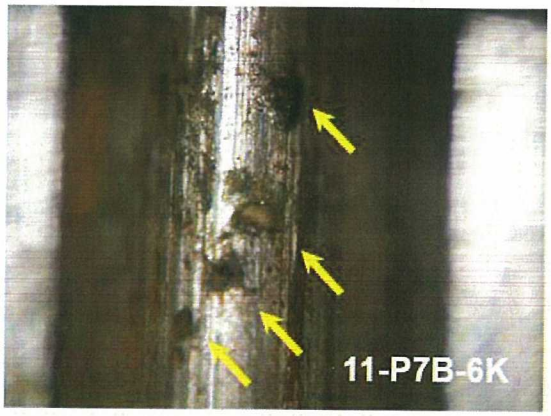

Pitting at root near middle of Coupling No. 6 (Stereomicroscopy 50X)

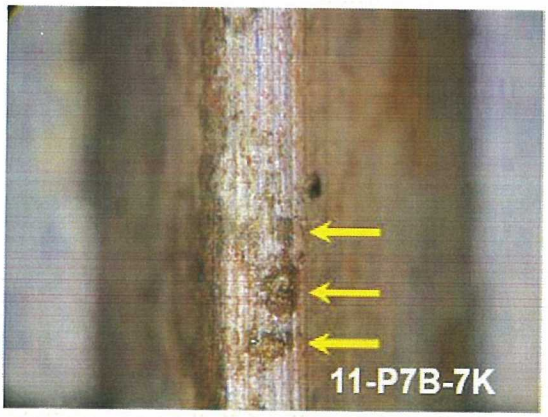

Pitting at root near middle of Coupling No. 7 (Stereomicroscopy 50X)

Figure 3-21: Pitting observed in couplings with cracks or fractures

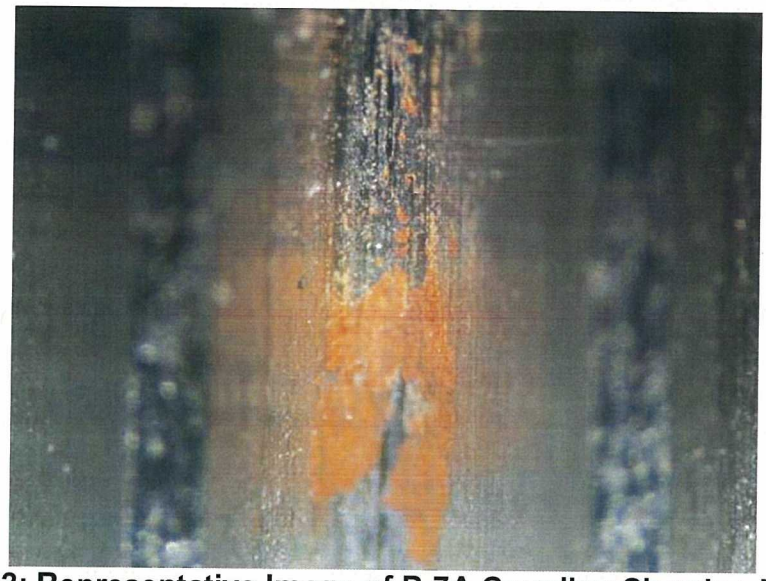

Figure 3-22: Representative Image of P-7A Coupling Showing No Pitting

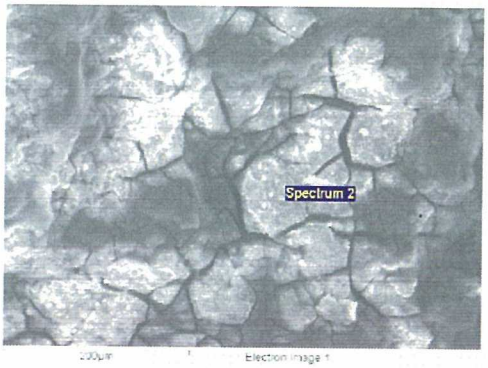

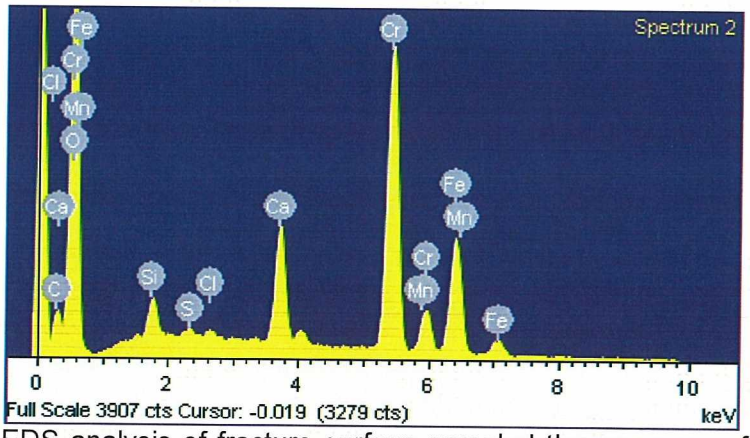

Element	Weight%
O	40.1
Si	1.7
S	0.3
Cl	0.3
Ca	5.9
Cr	29.5
Mn	0.4
Fe	Bal.

EDS analysis of fracture surface revealed the presence of corrosive agents (chlorides, oxides and sulfides), consistent with stress corrosion cracking. The high chromium level in the spectrum is likely attributed to local chromium carbides in the EDS sampling volume.

Figure 3-23: EDS of Coupling 11-P7C-6F Surface Deposit – Spectrum 2

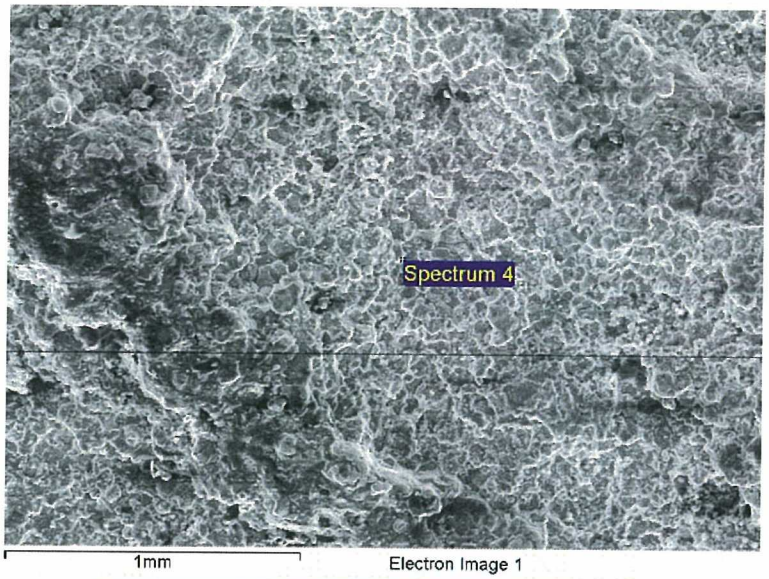

Element	Weight %
O	7.5
Si	0.9
S	0.3
Cl	0.3
K	0.2
Ca	0.4
Cr	14.6
Mn	1.6
Fe	Bal.

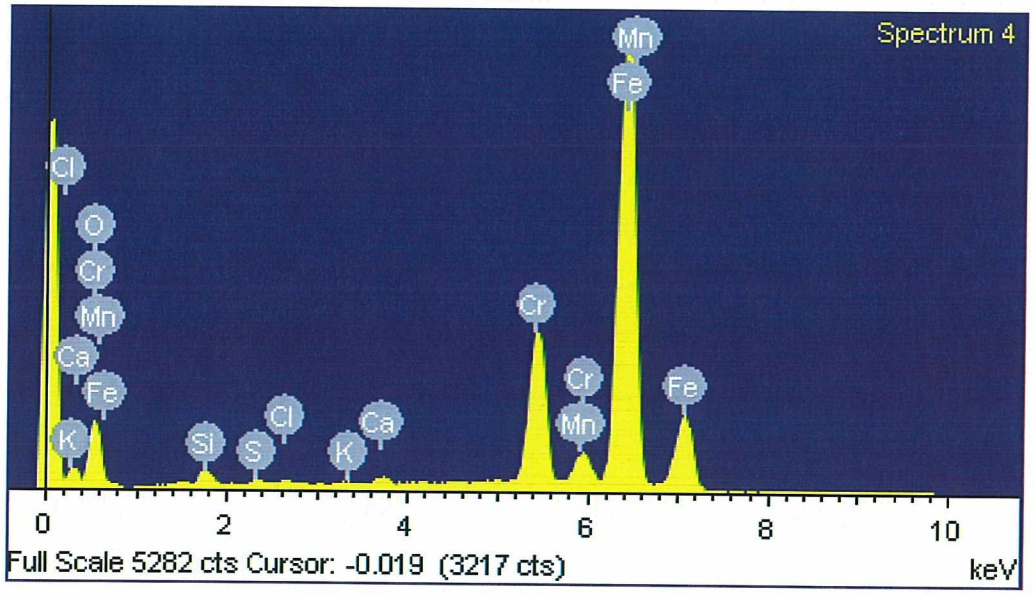

Figure 3-24: EDS of Coupling 11-P7C-6F Surface Deposit – Spectrum 4

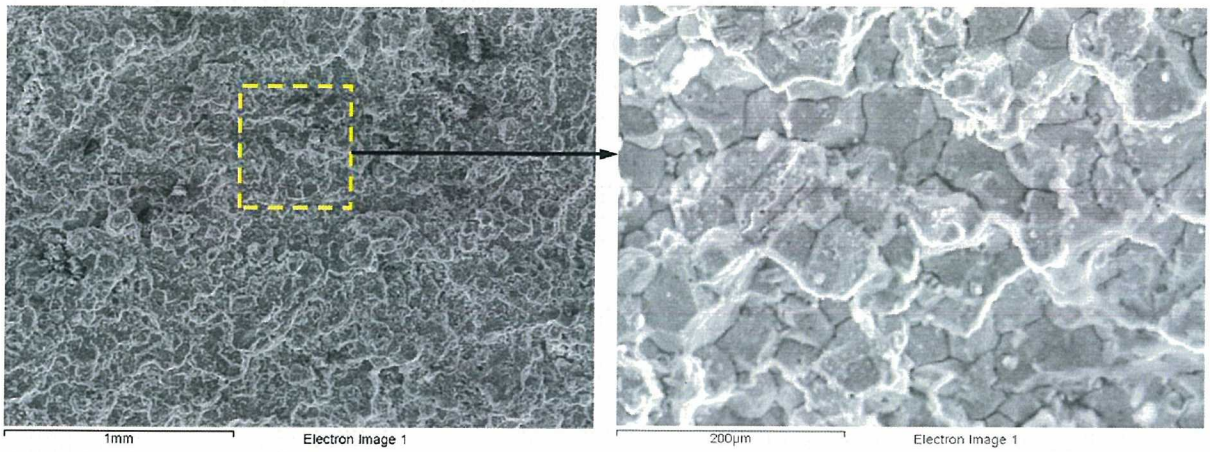

Fracture surface morphology exhibited a rock-candy appearance, characteristic of intergranular stress corrosion cracking. This is typical of a quench and tempered steel, such as a 400 series martensitic steel.

Figure 3-25: SEM of Coupling 11-P7C-6F Surface

4.0 DISCUSSION OF RESULTS/EVALUATION

Metallurgical examination and testing of failed couplings 11-P7C-6F and 09-P7C-7F, documented in Section 3.0, identified the failure mechanism to be stress corrosion cracking (SCC) and more specifically intergranular SCC (IGSCC). Stress corrosion cracking is a failure process of a material subjected to sufficient tensile stress in a corrosive environment for which the material is susceptible. IGSCC is SCC along grain boundaries. SCC "...is a subcritical crack growth phenomenon involving crack initiation at selected sites, crack propagation, and overload final fracture of the remaining section. Failure by SCC is frequently encountered in seemingly mild chemical environments at tensile stresses well below the yield strength of the metal. The failures often take the form of fine cracks that penetrate deeply in to the metal, with little or no evidence of corrosion on the nearby surface or distortion of the surrounding structure. Therefore during casual inspection no macroscopic evidence of impending failure is seen [24]."

Each of the three criteria 1) susceptible material, 2) corrosive environment and 3) tensile stress, considered to be necessary for SCC to occur, as it relates to the service water pump couplings, is discussed in the following subsections.

4.1 Susceptible Material

The coupling material was specified to be ASTM A582 Type 416 SS, tempered to a hardness in the Rockwell C range of 28 to 32 (HRC) [3c]. ASTM A582 Type 416 SS is a free-machining martensitic stainless steel with relatively high sulfur content that gives it excellent machining characteristics, while providing generally low corrosion resistance for a 12% chromium stainless steel.

ASTM standard A582 [7] provides chemical and hardness requirements for the coupling material. No requirements for toughness or tensile strength are provided in ASTM standard A582 [7]. Per ASTM A582 [7], the hardness range for 416 stainless in the tempered condition is 248-302 Brinell which equates to 24.2-32.1 HRC. The couplings were specified in the narrower 28 to 32 HRC range to mitigate the effects of galling during pump assembly and operation [4].

Heat treatment of the couplings to achieve the specified properties can be garnered from the heat traces provided in Attachment A. The heat traces provided in Attachment A are re-plotted for the hardening and tempering heat treatments and presented in Figure 4-1 and Figure 4-2. The re-plotted heat traces are in relative time with zero being the time at which the heat treatment started for each batch.

According to the heat treatment process described in Attachment VI of the root cause evaluation report for CR-PLP-2009-04519 [1] and the heat trace in Figure 4-1, the couplings were hardened by quenching (rapid cooling) using nitrogen in a vacuum furnace from approximately 1870°F that quickly cooled the parts to ambient. The microstructure transforms from austenite to martensite when the couplings are quenched. The ASM metals handbook [26] and heat treater's guide [25] recommends an austenitizing temperature in the range of 1695°F to 1850°F for 416 SS. The austenitizing temperature of 1870°F, exceeds the recommended maximum of 1850°F. The effect of austenitizing temperature on the as-quenched hardness of three martensitic grades is shown in the figure to the right (extracted from [26]). It shows that "the hardness increases with increasing austenitizing temperature to about 1800°F, then decreases because of austenite retention and (occasionally) the formation of delta ferrite. Certain subtle anomalies in these steels that should be considered before specifying a heat treating procedure are exemplified in the opposing injurious effects of the high and low extremes of austenitizing temperature, depending on the subsequent tempering temperature [26]." The ASM heat treater's guide [25], recommends using the low side of the austenitizing range when tempering is to exceed 565°C (1050°F), which would be applicable to the subject couplings given their tempering treatment.

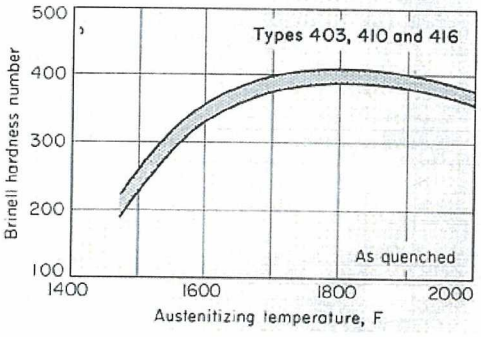

The ASM heat treating handbook [26] and guide [25], recommends a tempering temperature range of 1050°F to 1125°F for hardness in the range of 25 to 31 HRC. Also, "Tempering at 370°C to 565°C (700°F to 1050°F) [is] not recommended for parts requiring high toughness and optimum corrosion resistance. Causes a marked dip in impact resistance and lowered stress corrosion cracking resistance. Double tempering [is] beneficial. Cool to room temperature between tempers [25]." The effect of tempering temperature on the stress-corrosion characteristics of two martensitic stainless steels at a stress level of 80ksi in a salt fog cabinet is

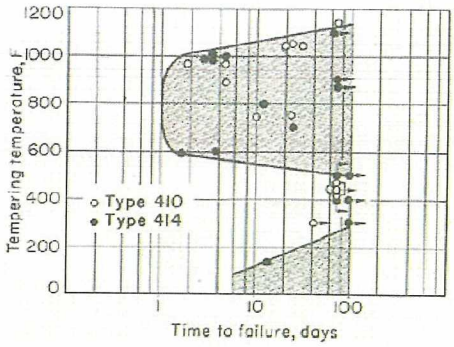

provided in the figure to the right [26].

Referring to the heat traces in Figure 4-2, the couplings were tempered in the range of 1025°F to 1090°F. This range encompasses a double temper. The double temper was performed to attain the specified hardness of 28 to 32 HRC. The first temper is in the range of 1050°F to 1080°F. Based on the first tempers, the austenitizing temperature of 1870°F (see Figure 4-1), not only exceeds the recommended maximum of 1850°F (as discussed above) but is on the wrong side of the recommended range.

Referring again to Figure 4-2, notice that the couplings extracted from P-7A were single tempered whereas the couplings installed and extracted from P-7B and P-7C were double tempered. Although double tempering could be beneficial, the second temper of the P-7C couplings under Hydro-Aire work order (WO) 202017 (yellow line) and 202067 (red line) were at approximately 1025°F, which is in the range that should be avoided.

Testing showed that surface hardness ranged from 24.5 to 33.6 HRC and through-thickness hardness measurements of 2011 extracted couplings ranged from 24.0 to 33.6 HRC. Through-thickness hardness measurements of coupling 09-P7C-6F ranged from 34.8 to 37.1HRC with an average of 36HRC. These through hardness values for coupling 09-P7C-6F are comparable to the results reported in Consumer Energy Lab Report 0900609 attached in [1]. Based on the surface and through thickness hardness testing results there is no correlation with couplings that were within the specified hardness range and couplings that were cracked or failed. That is, some couplings with out-of-specification hardness (e.g. 11-P7A-5) did not exhibit cracks whereas some couplings within specification (11-P7B-5K through -7K) exhibited cracks. Thus, out-of-specification hardness is not the root cause of observed cracks and failures.

No requirements for CVN impact test absorbed energy are specified in ASTM Standard A582. Nevertheless, the impact tests reveal low absorbed energy that indicates low fracture toughness of the coupling material. Low fracture toughness correlates to stress corrosion cracking (SCC) susceptibility.

Based on the material properties from metallurgical testing and heat treatment provided in Figure 4-1 and Figure 4-2 , it is concluded that the material is susceptible to SCC.

4.2 Corrosive Environment

The Service Water System (SWS) takes cooling water from Lake Michigan via pumps P-7A, P-7B and P-7C for the removal of waste and decay heat. For the period between January 2009 to August of 2011, service water basin level ranged from elevation 576' to 580'. For the same period, the water temperature ranged from 32°F to 76°F (see Section 2.1).

Chlorination occurs on a daily basis and consists of the addition of sodium hypochlorite (i.e. bleach) upstream of the traveling screens to control microbial species in the SWS. A water sample was taken by the Palisades chemistry department on 8/19/11 downstream of YS-0134 in the chemistry cold lab prior and post chlorination of the Service Water System. The chemistry water sample data is presented below.

	Pre Chlorination	Post Chlorination
Date/Time	8/19/2011 14:10	8/19/2011 18:48
Chlorination in Progress	No	Yes
Temperature	22.8 C	22.5 C
PH	8.30	8.21
Dissolved Oxygen	9 ppm	10 ppm
Chloride Concentration	9.72 ppm	10.2 ppm

This data indicates that chloride levels are relatively low and not significantly increased by chlorination of the service water. At these service water chloride concentrations, potential for pitting and SCC in the couplings is expected to take much longer for couplings that are continuously submerged than those in the wet/dry region. This is due to the intermittent nature of the service water pumps and the alignment hole, whereby couplings above the normal water basin will experience wet/dry cycles that can concentrate chlorides and other corrosive anion species on the middle thread surfaces (where the shafts touch). Visual examination of failed coupling 11-P7C-6F supports this hypothesis with corrosion product staining on the area below the alignment hole and on the center internal threads found to have cracks.

4.2.1 Effect of Neolube

The couplings threaded surfaces were observed to be coated, to varying degrees, with lubricant during the visual inspection (see Section 3.1). Per PLP work instructions WI-SWS-M-03 [30] and WI-SWS-M-04 [31], Neolube

No. 1 is applied to the threaded surfaces of the pump shaft during the assembly of the shaft.

Neolube No. 1 is a dry, conductive lubricant film, used extensively at nuclear facilities to prevent seizing, fretting, galling and resists abrasion of rubbing surfaces.

According to work instructions WI-SWS-M-03 [30] and WI-SWS-M-04 [31], Neolube No. 1 is to be applied to the shaft threads during assembly of the pump shaft. The work instruction for P-7A, WI-SWS-M-03 [30], excludes application of Neolube No. 1 on the three threads nearest the end of line shafts. The work instruction for P-7B and P-7C, WI-SWS-M-04 [31], does not provide such exclusion on application of Neolube No. 1. A review of WI-SWS-M-03 Revision 0, which was applicable for the extracted P-7A couplings, indicates the same exclusion of Neolube, without specific mention of "No. 1", on the three threads nearest the ends.

Visual inspection of the as-split P-7A couplings (see Section 3.1.2) revealed Neolube application inconsistent with the work instruction [30]. As-split P-7A couplings exhibited generous amounts of Neolube on the threads, including the center of the coupling. Neolube at the center of the couplings would not be expected if the last three shaft threads were not coated. Visual inspection of the as-split P-7B and P-7C couplings indicated less Neolube compared to P-7A. No cracks were observed by MT on tested P-7A couplings.

The potential for corrosion as a result of application of this lubricant to the shaft and coupling arises from the composition of Neolube. Neolube No. 1 is composed of 99% pure furnace graphite particles in isopropanol with a thermoplastic resin binder (see technical datasheet in Attachment A). Graphite, due to its position on the galvanic series is known to attack stainless steel and other less noble metals [35]. The article presented in [34], also suggests that lubricants containing graphite should not be in contact with stainless steels in seawater. However the percentage of graphite by weight in Neolube is relatively small, approximately 2.5% (3.3% total solids content x 75% graphite content = 2.5%). For galvanic corrosion there typically needs to be more noble material than less noble.

It is postulated that the thermoplastic binder in Neolube inhibits corrosive species in the service water environment from attacking the coupling material. The percentage of graphite in Neolube (~2.5% overall) is not sufficient to attack the couplings unless the thermoplastic binder is washed

away while the graphite remains. In this case, a local galvanic cell could be established when water drains from the coupling and only a small amount of electrolyte is present on the coupling.

Although the effect of Neolube on pit formation and SCC in the couplings is not clear, no cracks or pits were found in P-7A couplings that received a generous coating of Neolube. This evidence suggests that the small amount of graphite present in Neolube did not corrode the coupling material and, in fact, the Neolube composition might actually serve as an inhibiter to corrosive species in the service water. To better understand the effects of Neolube on couplings, further testing would be required.

4.3 Tensile Stress

The fracture surface revealed that coupling 11-P7C-6F failed due to stress corrosion cracking initiating from two initiation sites (pits) in the thread root and propagating in a semi-elliptical manner perpendicular to the coupling axis through the thickness until overload of the remaining ligament. To support this failure mechanism, an evaluation of the coupling stresses was performed to determine if tensile stresses are sufficient to initiate SCC.

The function of the couplings is to couple the various segments of shafts (i.e. line shafts, packing shaft and motor shaft) together in order to transmit the motor torque to the impeller approximately 40 feet below. The design of the couplings is such that the shaft ends can bear against each other, which can lead to tensile and shear stresses across the coupling.

The couplings and shafts are assembled to ensure equal threading of the two shafts within a coupling by the use of an alignment aid inserted in the 1/8" hole on the side of the coupling. Once the shafts touch the alignment aid, it is removed and, then, motor torque is relied upon to tighten up the shaft-coupling assembly. With application of motor torque, it is postulated that the two shafts will tighten and bear against each other within the coupling (see Figure 4-4) which will induce compression on the shaft. The shaft compression is reacted as tension across the coupling. Also when the shafts butt up against each other within the coupling, a circumferential gap between the shaft and coupling is created due to the end geometry of the two shafts. The gap in conjunction with the alignment hole would enable deposits to collect at the exposed thread roots of the shaft intersecting plane.

To estimate the tensile stresses across the couplings, a finite element analysis (FEA) model of the coupling was created in ANSYS [13]. ANSYS is

a multipurpose finite element analysis software program and is verified and validated in accordance with LPI Procedure 4.1 [16], as documented within [17].

4.3.1 FEA Model Description

A half FEA model of an intact coupling was developed using ANSYS and consists of the steel body, alignment hole and threads. The model was constructed of the eight-node brick element, SOLID45 (see Figure 4-5). The symmetric boundary condition, $U_z=0$ and $U_\theta=0$, is applied on the inner surface as shown in Figure 4-6.

ASTM A582 Type 416 stainless steel material properties for the coupling FEA model are as follows:

Young's modulus: 29.2×10^6 psi
Poisson's ratio: 0.3

Coupling threads are 2-3/16, 8 TPI (see Figure 1-5), which is not a common thread form. Specific thread properties are not available in the Machinery's Handbook [14]. Therefore, internal thread properties of the coupling are taken to be the average internal diameter of 2-1/4, 8 TPI and 2-1/16, 8 TPI per the Machinery's Handbook [14].

4.3.2 Loading Condition

Loading on the coupling model consists of the weight of components below the coupling, hydraulic thrust and motor torque. The loads are extracted from HydroAire calculation NQ5940 [15].

Two motor torque loading scenarios (MTS) are considered for transmittal of the motor torque across the coupling: 1) motor torque is transmitted across the coupling from shaft to coupling purely by thread friction (MTS1; see Figure 4-3) and 2) motor torque is transmitted across the coupling by bearing of the shaft ends against each other within the coupling (MTS2; Figure 4-4). To simulate uneven shaft alignment within the coupling, a bending moment is also considered as a load. These loads are combined as follows for evaluation of the couplings.

Load Combination 1 (LC1) = Weight + Thrust + MTS1

For this load combination, component weight and hydraulic thrust is combined with the motor torque loading scenario 1 (MTS1) in which motor torque is transmitted across the coupling purely by friction. Axial

thrust, F = 8,780 lb, is evenly distributed on the nodes at the inner surfaces of each thread (see Figure 4-7). Torque, T=18694 in-lb [15], is first converted into circumferential force, F by T=F*R where R is the coupling friction radius and then evenly applied on the same nodes that the axial thrust load is applied.

Load Combination 2 (LC2) = Weight + Thrust + MTS2

For this load combination, the weight and axial thrust is applied in the same manner as in LC1. Bearing of the shafts within the coupling will induce tensile stress across the coupling. The tensile force of 42 kips is evenly distributed to the first three threads from the contact plane of the two shafts (see Figure 4-8). Typically with threaded connections, the first few threads near the plane of induced load carry the majority of this load [18]. For this assessment, the first three threads were considered to carry the load.

Load Combination 3 (LC3) = Weight + Thrust + MTS2 + Moment

For this load combination, loads are applied in the same manner as LC2 with the addition of a moment on the coupling to account for misalignment or other postulated scenarios that can induce bending across the coupling. A bending moment equivalent to 20% of the stress induced by MTS2 of approximately 4,962 in-lb (see below) was also applied to the coupling. This moment was converted into axial force, Fz, and applied on the nodes on the end cross-section based on the nodes' y direction distance from center (see Figure 4-9).

$OD := 3.187 \cdot in$ Out diameter of coupling

$ID := \frac{(2.125 + 2.25) \cdot in}{2}$ Internal diameter of coupling

$Sp := \frac{\pi \cdot (OD^2 - ID^2)}{4}$ Area of cross-section of coupling

$Fp := 42335 \cdot lb$ Clamping force

$\sigma := \frac{Fp}{Sp}$

$Ip := \left(\frac{\pi}{64}\right) \cdot (OD^4 - ID^4)$ Area moment of inertia of coupling

$Mom := 0.2\sigma \cdot \frac{Ip}{\frac{OD}{2}}$

$Mom = 413.5\,lb\,ft$ Moment can result in 20% stress result from clamping force

4.3.3 FEA Results

1) LC1: In this case, the circumferential stress, axial stress and first principal stress are relatively low due to the even distribution of loads on the coupling (see Figure 4-10). Axial tensile stresses at the thread root are on the order of 3.5 to 5 ksi. This result indicates that if the motor torque is transmitted across the coupling purely by thread frictional resistance, then the coupling tensile stresses are relatively low.

2) LC2: This load combination results in high stress concentrations at the thread root of the coupling at the contact plane of the two shafts. Axial tensile stresses at the thread root are over 10 times greater than LC1 with stresses on the order of 60 to 70 ksi. The stress distribution at the middle thread root across the coupling wall for this load combination root is presented in Figure 4-12.

3) LC3: This load combination does not significantly increase stresses at the thread root of the coupling from LC2. The additional bending moment on the coupling produces additional stresses on the outside diameter of the coupling. However it does not appreciably increase stresses at the thread root where SCC initiation is observed.

Average tensile stresses at the first thread root for each load combination is summarized in the matrix below.

Load Combination	Average Tensile Stress (psi)
LC1: No Bearing	3,790
LC2: Shaft Bearing	60,506
LC3: Bearing Shaft and Bending	60,476

The limiting load combination is LC2. The resulting tensile stress indicates that the failure was not a single overload event since the average yield and tensile strength are approximately 136 ksi and 151 ksi (see Section 3.6), respectively.

The Figure 4-12 stress distribution is based on reacting the applied shaft end compression load from the applied motor torque across three threads[3] per shaft end. Considering the two shafts meeting approximately in the center of the coupling, the three threads below the centerline react the lower shaft compression loading, the three threads above the centerline react the compression loading in the upper shaft. However, tolerances in machining of the threads could translate into different load and stress distribution across the threads. If the load is distributed to fewer or greater number of threads than the three assumed, then the tensile stress at the thread root could range according to the load distribution to the threads.

For example, if the shaft bearing loads were distributed across six threads instead of three, the maximum tensile stress would be on the order of 30 ksi. Based on the FEA and depending on the number of threads sharing the load, it is not un-reasonable for tensile stresses to range from approximately 20 ksi to 80 ksi at the thread root.

4.4 SCC Process

The time to failure of a susceptible material in a given environment is dependent on the applied tensile stress, as shown in the Figure 4-14 schematic. The plot compares applied stress or load to the logarithm of exposure time in an environment and illustrates the time to failure increases significantly with decreasing applied stress. The crack propagation time, t_{cp} is taken to be the difference between the time of failure, t_f, minus the time of initiation, t_{in}. The time at failure is typically known. However, the time of

[3] Based on extensive testing, as presented in various literature sources [32], the threads nearest the plane of load application carry the majority of the applied loading.

initiation is highly alloy-environment and applied stress dependant and thus is an unknown without specific test data. The initiation time is also highly dependent upon pre-existing flaws that may have been introduced during heat treatment or thread fabrication. Therefore, predicting initiation time is difficult. Unless there are preexisting flaws, a distribution of 80% initiation and 20% propagation is considered reasonable for the life of a component subject to SCC process as suggested by Figure 4-15.

The SCC process usually occurs in three stages:

1) crack initiation and stage 1 propagation,
2) stage 2 or steady-state propagation (independent of stress intensity), and
3) stage 3 crack propagation or final fracture.

A typical plot of crack growth rate (da/dt) versus stress intensity illustrating the three stages of SCC propagation is presented in Figure 4-16. The figure illustrates a threshold stress-intensity, K_{1SCC}, for SCC initiation and stage 1 propagation. The threshold stress-intensity is dependent upon interaction of the alloy and environment (alloy-environment). Stage 1 propagation is followed by Stage 2 crack propagation where the crack growth velocity is independent of stress intensity. Stage 2 crack growth velocity is limited to the alloy-environment interaction such as the mass transfer of corrosive environmental elements up the crack to the crack tip.

Stage 3 propagation is dependent upon stress intensity, until the critical level, K_{1c} to produce mechanical overload of the remaining ligament. The crack propagation time is the sum of the time at each stage, $t_{cp}=t_1+ t_2+ t_3$.

A plot of crack growth rate (da/dt) versus stress intensity for 12% chromium and 0.2% carbon alloy at various tempering temperature per [22] is provided in Figure 4-17. The generic categorization of 12% Cr and 0.2% C would cover the 416 SS coupling material. Based on tempering heat traces for the extracted service water couplings presented in Figure 4-2, the 550°C (1022°F) curve is appropriate. Figure 4-17 shows that the threshold stress-intensity, K_{1SCC} for the 550°C curve is approximately $20Mpa\sqrt{m}$ $(\sim 18ksi\sqrt{in})$ and the stage 2, stress intensity independent crack growth rate is approximately 2.3E-4 in/hr per [22].

For a stress distribution of 20 to 80 ksi, the stress intensity at the thread root (without pits) of the coupling can range from $6ksi\sqrt{in}$ to $26ksi\sqrt{in}$ as demonstrated below.

$j := 0..3$

$d_{thread} = 0.068\,in$ Thread height

$a := \frac{d_{thread}}{2}$ $a = 0.034\,in$ Load assumed to act at center of threads.

$\sigma_j :=$

20ksi
55ksi
70ksi
80ksi

$K_j := \sigma_j \cdot \sqrt{\pi \cdot a}$ [33] $K_j =$

6.5	$ksi\cdot\sqrt{in}$
17.9	
22.8	
26.1	

Therefore, based on three threads taking the load and resulting tensile stress of 70 ksi (see Figure 4-12), the stress intensity of $23ksi\sqrt{in}$ would be sufficient to initiate a crack. If the tensile stress at the thread root is 55 ksi or less, then the stress intensity would fall below the threshold stress intensity, K_{1SCC} of $18ksi\sqrt{in}$ and SCC initiation would not be expected. However, if a pit were to form at the thread root, the stress intensity would be higher for a given tensile stress. For example, a pit 0.01" deep and tensile stress of 55 ksi would result in a stress intensity of approximately $24ksi\sqrt{in}$ (see below), which is greater than the threshold stress intensity for SCC initiation.

$Q := 0.9$ $M := 1$

$d_{pit} := 0.01\,in$ Assumed pit depth

$a := d_{pit} + a$ $a = 0.044\,in$

$\sigma_j :=$

20ksi
55ksi
70ksi
80ksi

$K_j := 1.12\,\sigma_j \cdot \sqrt{\frac{\pi \cdot a}{Q}} \cdot M$ [33] $K_j =$

8.8	$ksi\cdot\sqrt{in}$
24.1	
30.7	
35	

Once a crack initiates, the stress intensity would increase with increasing crack length, however the crack rate is limited to the stage 2 propagation rate until the critical fracture stress intensity, K_{1c} resulting in overload failure.

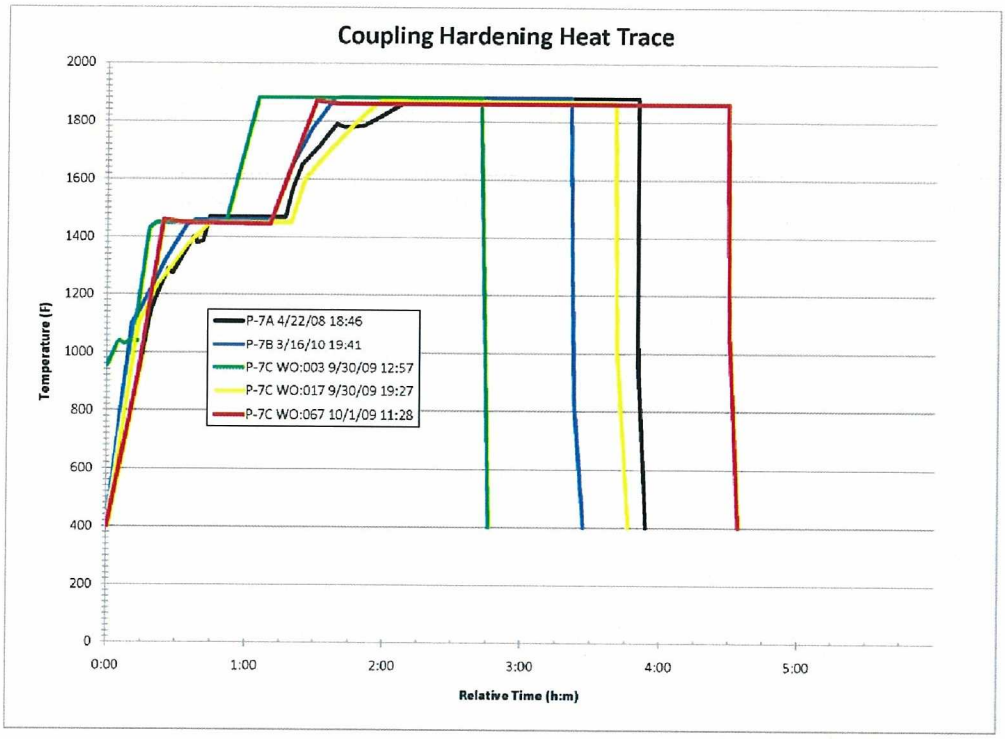

Figure 4-1: Hardening Heat Traces

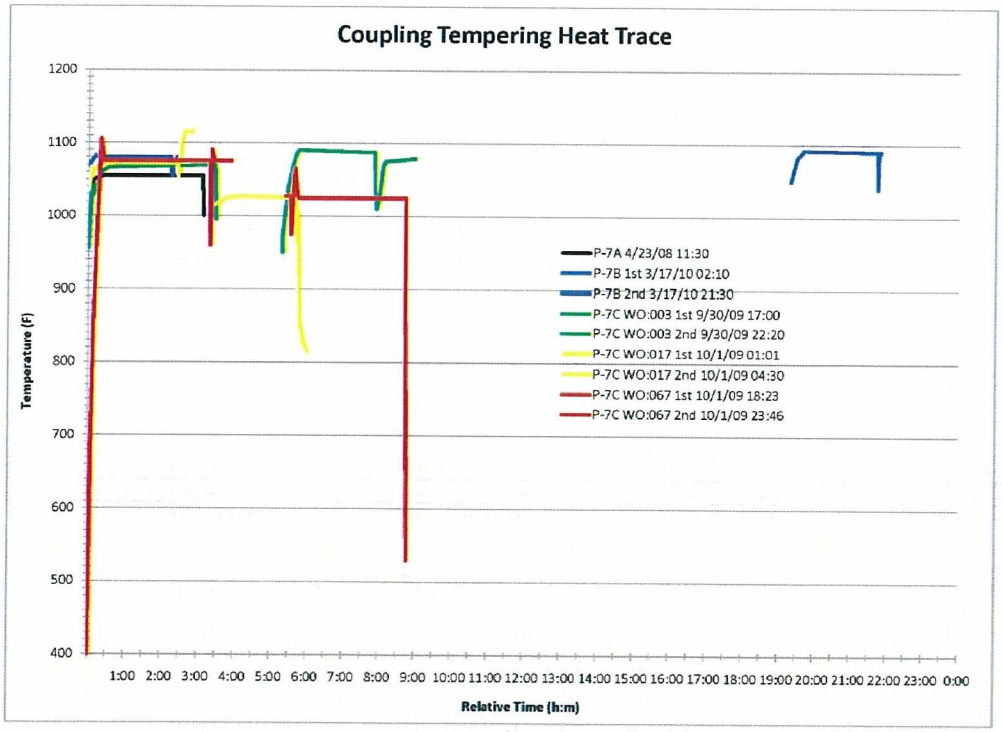

Figure 4-2: Tempering Heat Traces

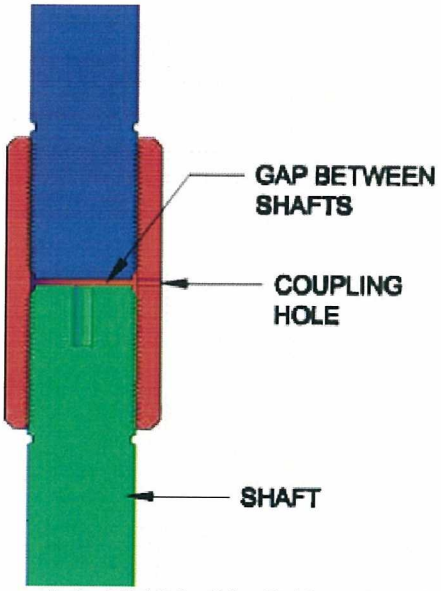

Figure 4-3: MTS1: Shaft Not Bearing

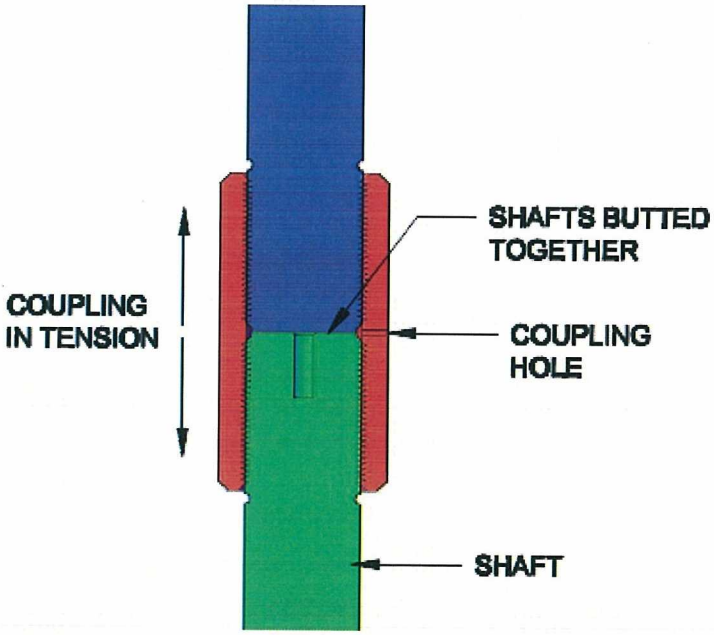

Figure 4-4: MTS2: Shaft Bearing

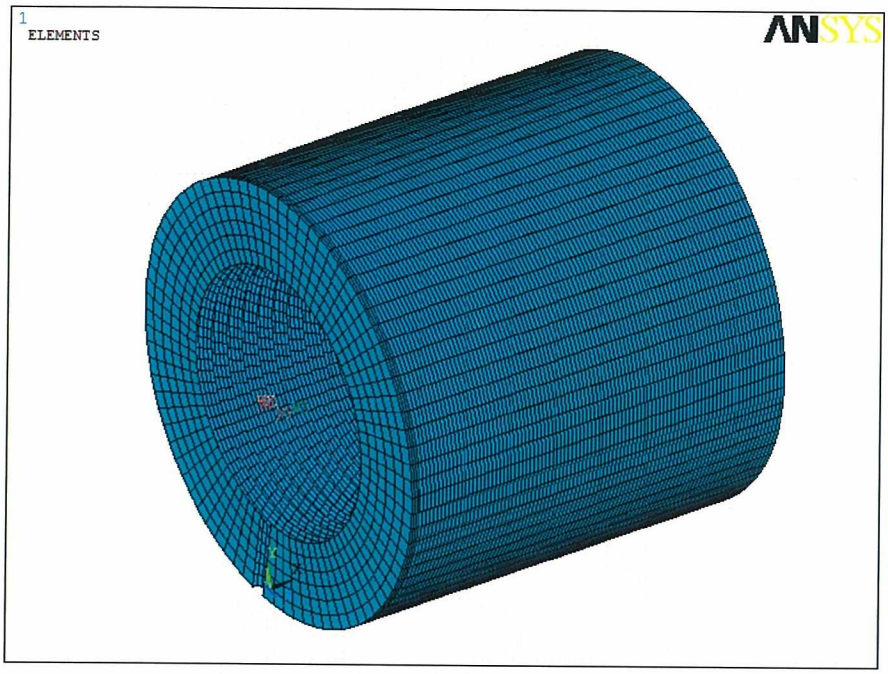

Figure 4-5: Half FEA model of coupling

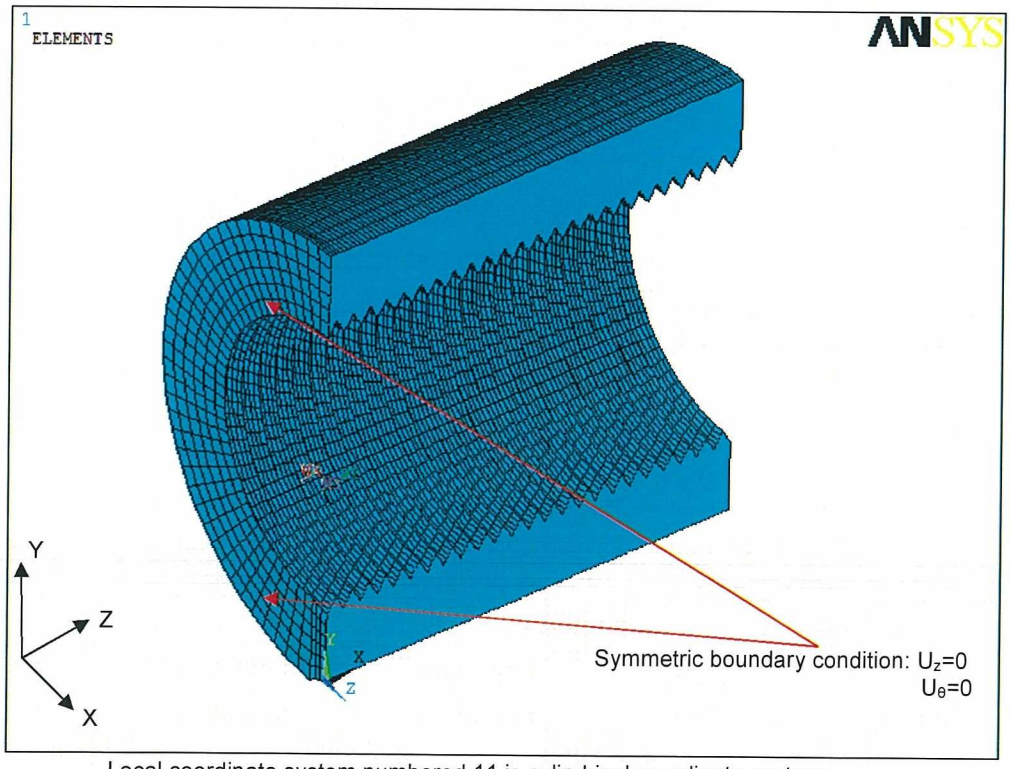

Local coordinate system numbered 11 is cylindrical coordinate system

Figure 4-6: Cross-section of half FEA coupling model

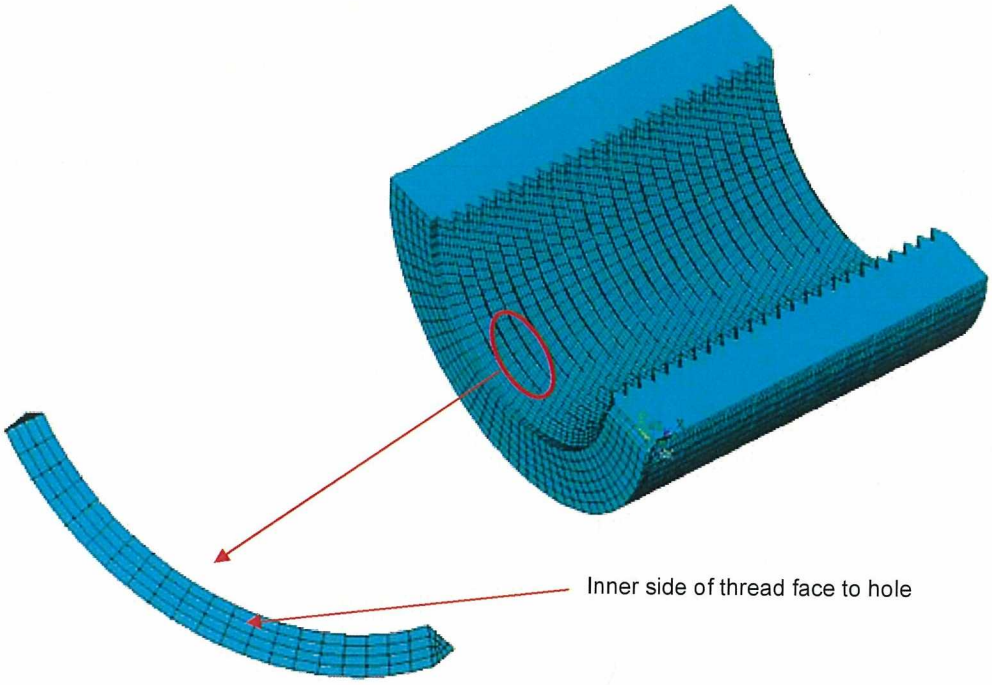

Figure 4-7: Load application Sketch of loading condition in no bearing case

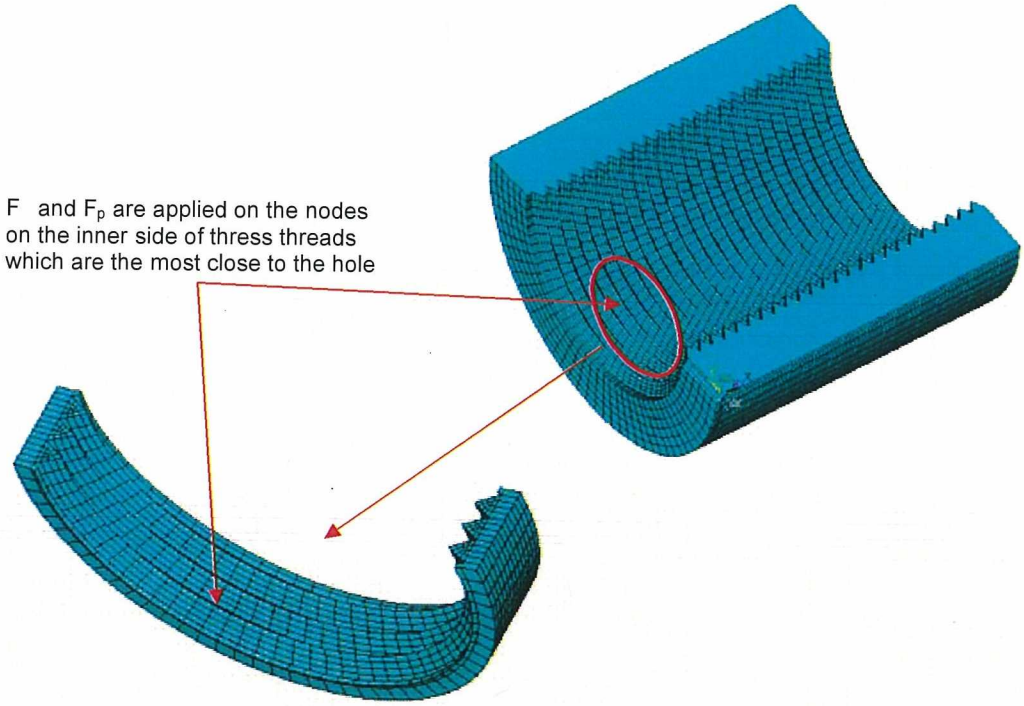

Figure 4-8: Sketch of loading condition in shafts bearing case

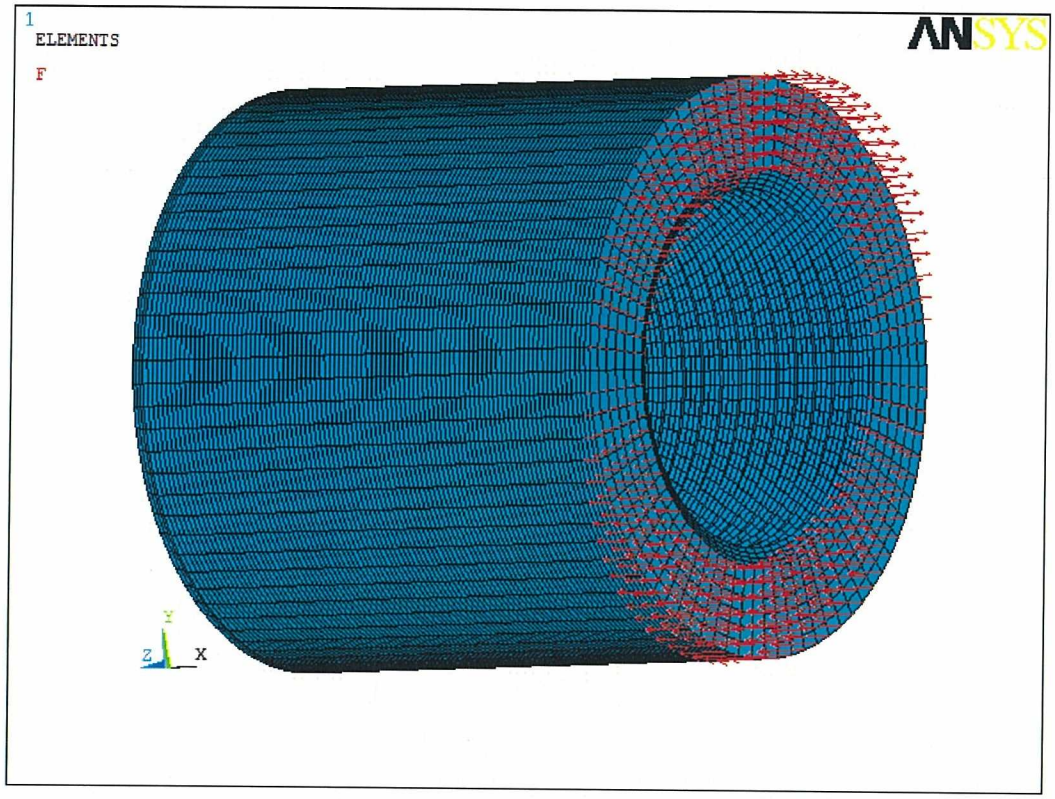

Figure 4-9: Sketch of axial force result from bending moment

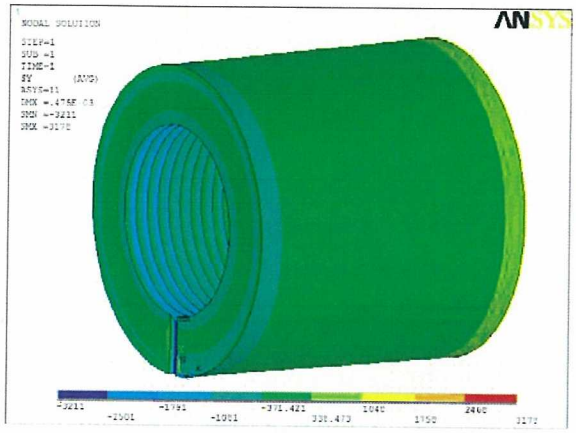

Circumferential Stress

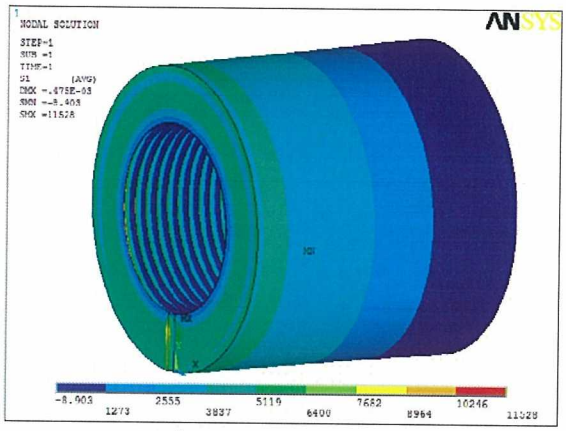

1st Principal Stress

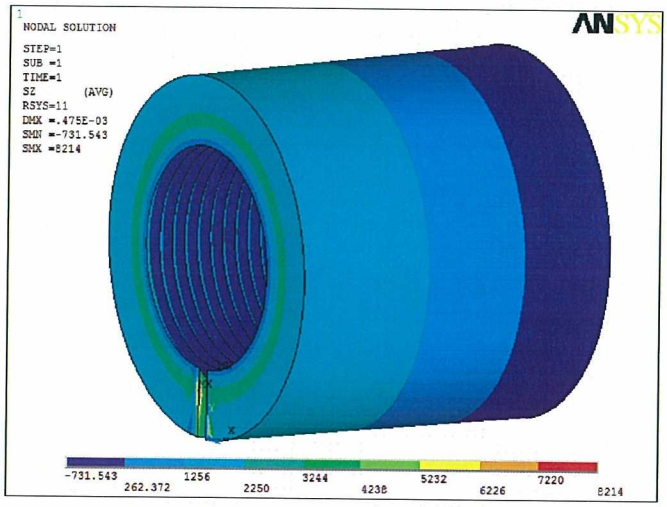

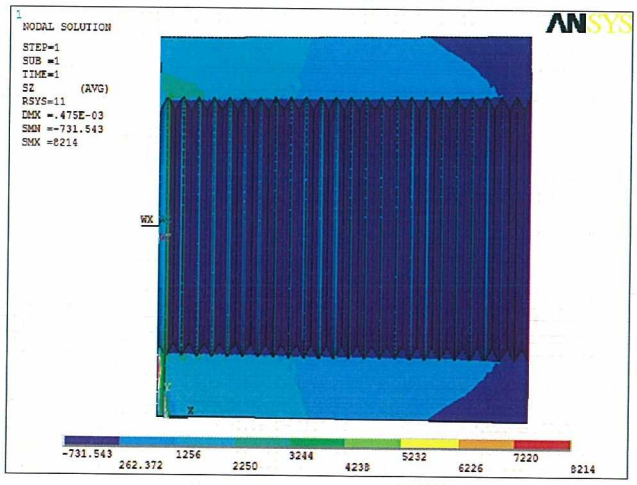

Axial Stress

Figure 4-10: Resultant stresses for LC1

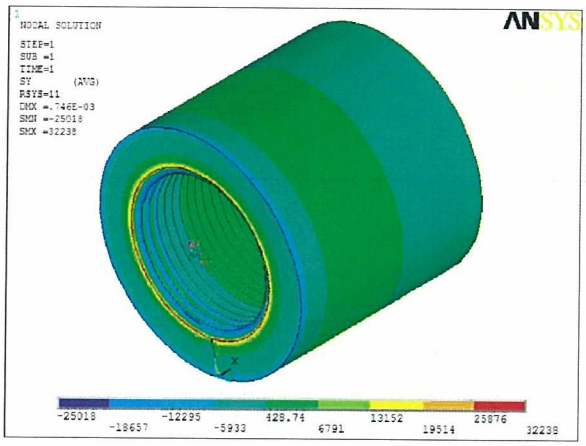

Circumferential Stress

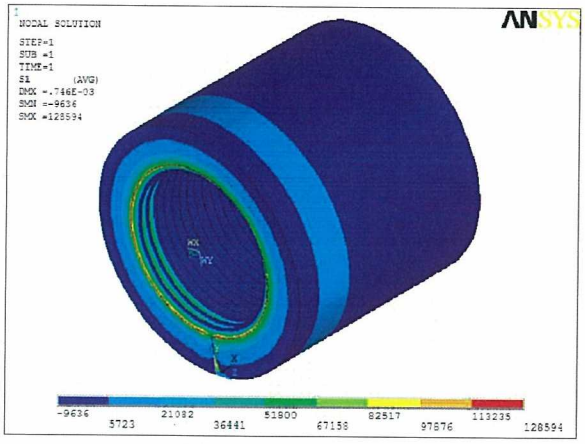

1st Principal Stress

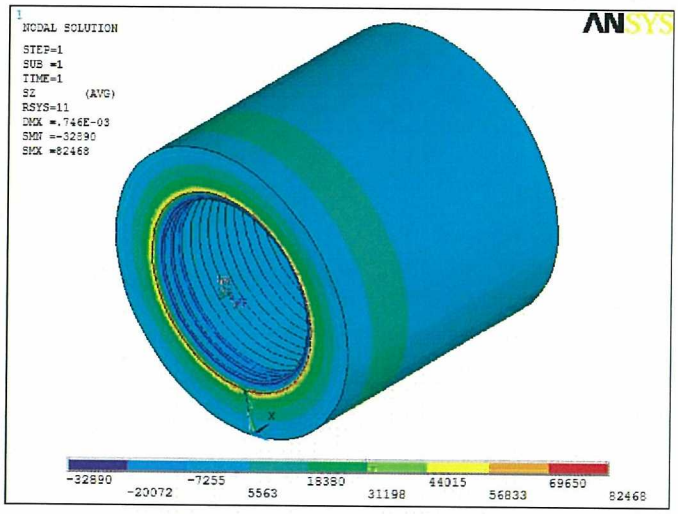

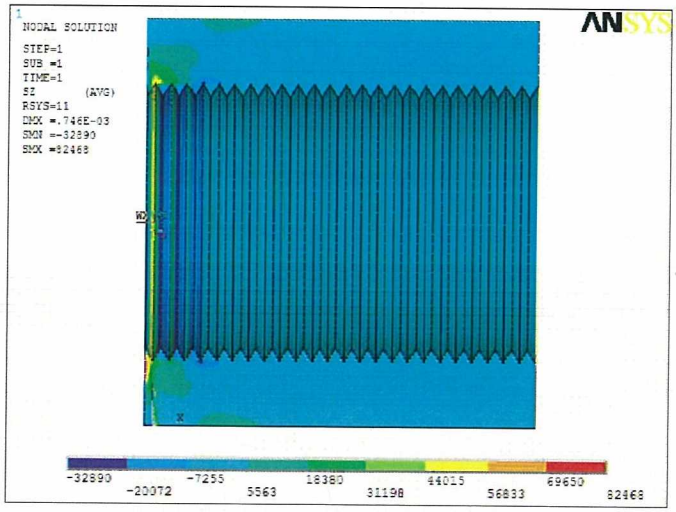

Axial Stress

Figure 4-11: Resultant stresses for LC2

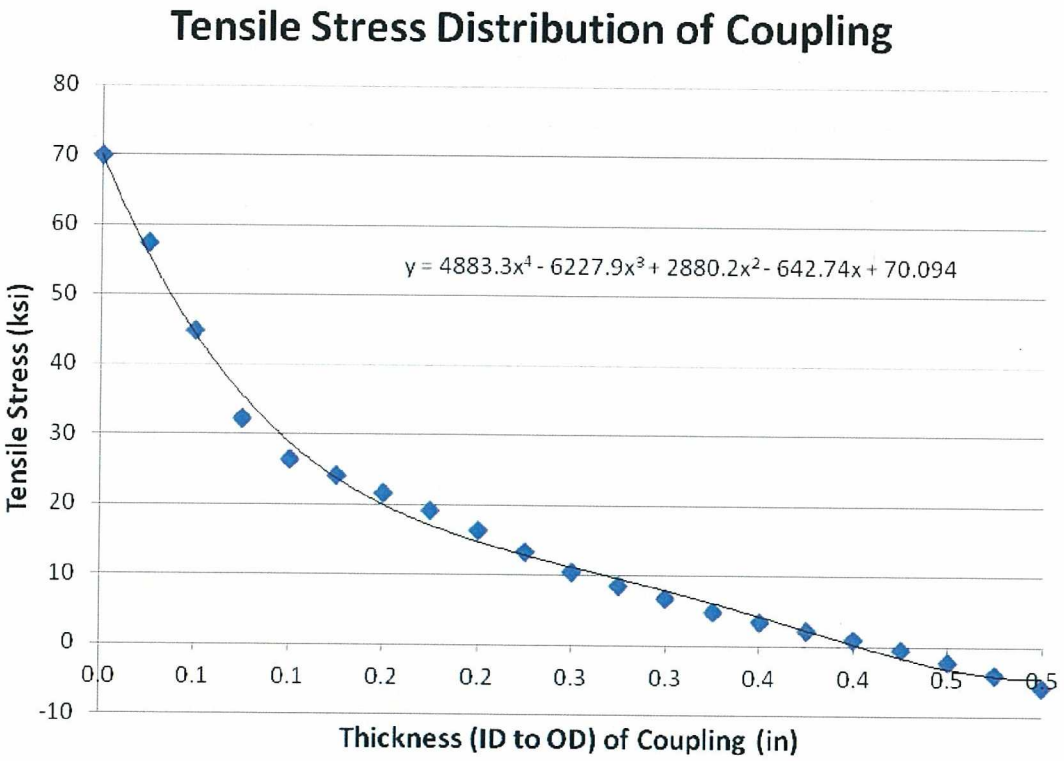

Figure 4-12: Tensile Stress Distribution Across Wall Thickness of Coupling – LC2
(Based on three threads reacting out applied load)

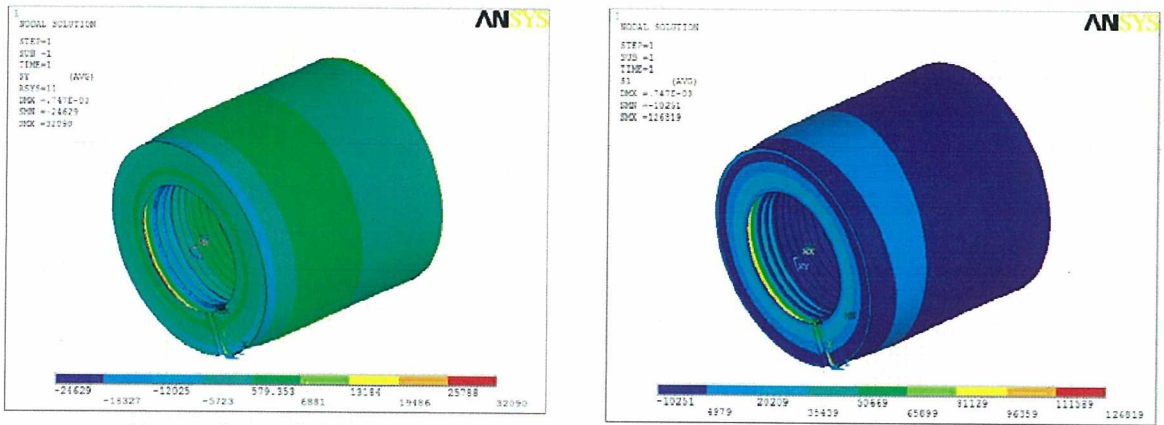

Circumferential Stress

1st Principal Stress

Axial Stress

Figure 4-13: Resultant stresses for LC3

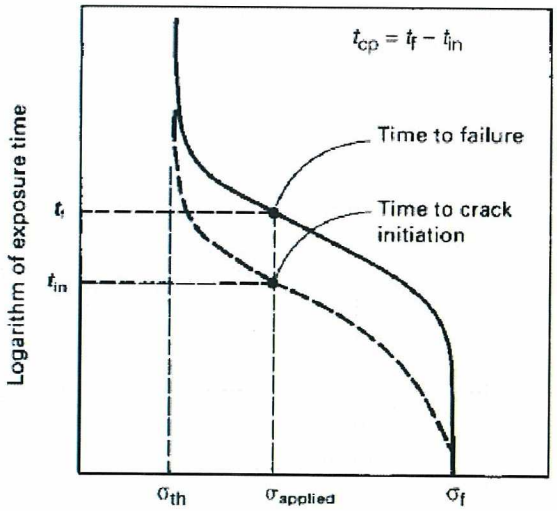

Figure 4-14: Time to Failure vs Applied Stress [23]

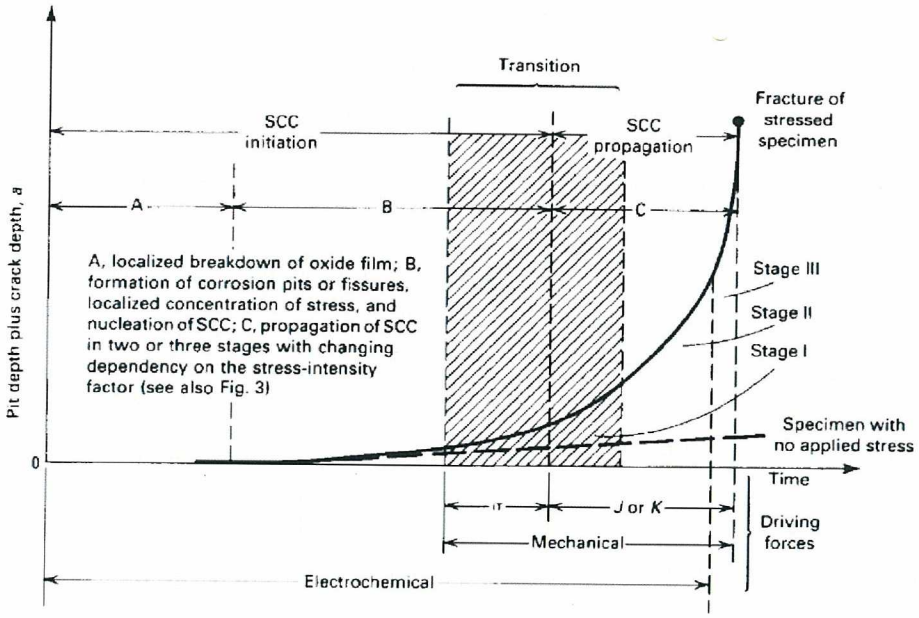

Fig. 2 The relative influences of electrochemical and mechanical factors in the corrosion and SCC damage of a susceptible material. The shaded area represents the transition of driving force from dominance by electrochemical factors to chiefly mechanical factors. Precise separation of initiation and propagation stages is experimentally difficult. Stimulation of cracking by atomic hydrogen may also become involved in this transition region.

Figure 4-15: SCC Process [28]

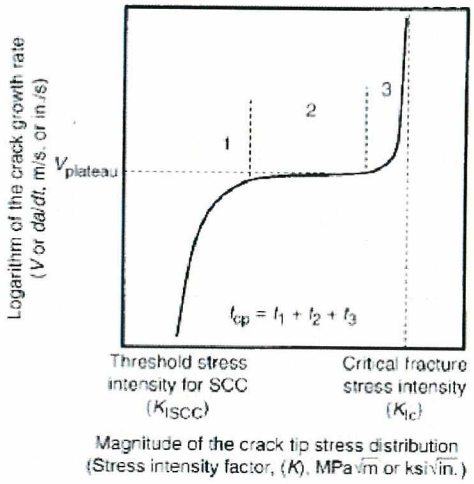

Figure 4-16: Crack Growth Rate (da/dt) versus stress intensity w/Three Stages of Crack Growth [23]

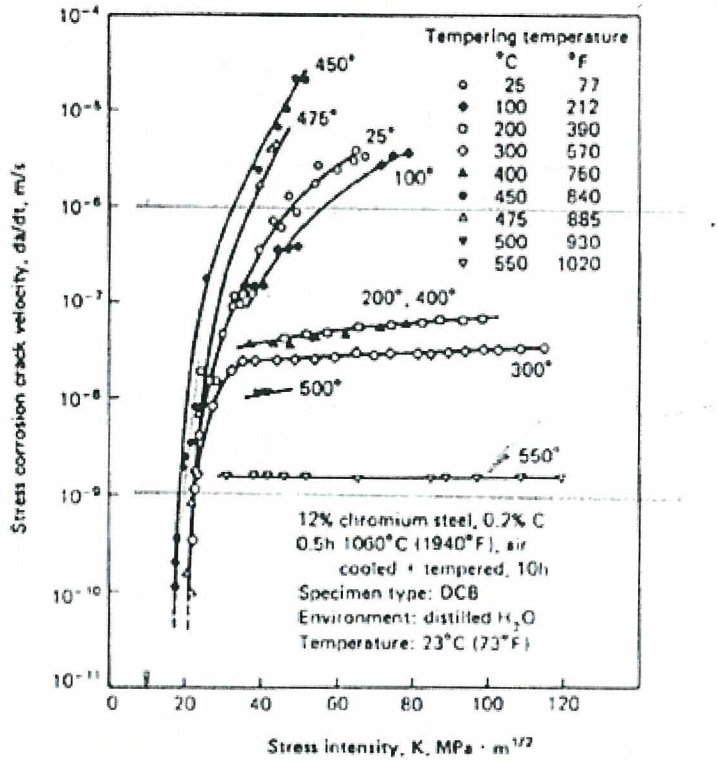

(b) Crack velocity for a 12% chromium steel in distilled water.

Figure 4-17: Effects of Tempering Temperature and Applied Stress-Intensity factor on Velocity of Stress-Corrosion Cracking [22]

5.0 SUMMARY/RECOMMENDATION

In August 2011, a Type 416 stainless steel (SS) coupling fractured in Service Water System (SWS) pump P-7C at Palisades Nuclear Plant (PLP). A previous coupling fracture occurred in the same pump in 2009. As a result of the recent failure, some couplings extracted from all three pumps at the PLP site were examined by magnetic particle testing that revealed four additional cracked couplings from pumps P-7C and P-7B, but not P-7A.

Metallurgical analysis of fractured and cracked couplings revealed that the failure mechanism involved intergranular stress corrosion cracking (IGSCC) along the prior austenite grain boundaries. This cracking mechanism is common for martensitic stainless steels exposed to chloride-containing environments.

Susceptibility of martensitic stainless steels to SCC is known to be dependent on tempering temperature. A review of heat treatment records for the couplings showed a first temper around 1075°F to 1100°F and, for the P-7B and P-7C couplings, a second temper at 1025°F. The second temper was performed because the resulting hardness following the first temper was not within the specified value of 28 to 32 HRC. Literature findings show that martensitic stainless steel alloys tempered around 1050°F are particularly susceptible to corrosion and SCC [25, 26]. The specified heat treatment required to achieve the designed hardness (28-32 HRC) and strength makes this martensitic stainless steel particularly susceptible to corrosion and SCC. Furthermore, the heat treatment did not conform to recommendations in the ASM guides for heat treating Type 416 SS as prescribed in [25, 26]. The austenitizing temperature of 1870°F exceeded the maximum recommended range of 1695°F to 1850°F and were on the wrong side of the range when considering the tempering temperatures in the range of 1050°F to 1080°F. That is, per ASM guides [25, 26] austenitizing temperatures should be on the low side, when tempering above 1050°F. A second temper was performed on couplings installed in P-7B and P-7C at 1025°F, which is in the range not recommended by ASM of 700°F to 1050°F [25, 26] that typically results in temper embrittlement and SCC. The heat treatment experienced by the couplings, which did not strictly conform to ASM guidelines [25, 26], increased the materials susceptibility to corrosion and SCC.

Cracks emanated from thread root regions and were predominantly found at the center of couplings that was exposed to a service water environment containing chlorides. Chlorides are known to cause pitting and SCC in martensitic stainless steels [29]. Couplings exhibiting cracks were also subjected to wet and dry cycles that could significantly increase concentrations of chloride species on the threaded surfaces due to the alignment hole enabling ingress and egress of water with